SANDIA REPORT
SAND2017-1828
Printed February 2017

Properties of Syntactic Foam for Simulation of Mechanical Insults

Neal B. Hubbard
Kimberly K. Haulenbeek
Matthew A. Spletzer
Lyndsy E. Ortiz

Prepared by
Sandia National Laboratories
Albuquerque, New Mexico 87185 and Livermore, California 94550

Sandia National Laboratories is a multi-mission laboratory managed and operated by Sandia Corporation, a wholly owned subsidiary of Lockheed Martin Corporation, for the U.S. Department of Energy's National Nuclear Security Administration under contract DE-AC04-94AL85000.

Issued by Sandia National Laboratories, operated for the United States Department of Energy by Sandia Corporation.

SAND2017-1828
Printed February 2017

Properties of Syntactic Foam for Simulation of Mechanical Insults

Neal B. Hubbard
Weapon Analysis, 00432
Sandia National Laboratories
P.O. Box 5800
Albuquerque, New Mexico 87185-0405

Kimberly K. Haulenbeek and Matthew A. Spletzer
Experimental Environment Simulation, 01528
Sandia National Laboratories
P.O. Box 5800
Albuquerque, New Mexico 87185-0557

Lyndsy E. Ortiz
Mission Support Communications, 3644
Sandia National Laboratories
P.O. Box 5800
Albuquerque, New Mexico 87185-0909

Abstract

Syntactic foam encapsulation protects sensitive components. The energy mitigated by the foam is calculated with numerical simulations. The properties of a syntactic foam consisting of a mixture of an epoxy-rubber adduct and glass microballoons are obtained from published literature and test results. The conditions and outcomes of the tests are discussed. The method for converting published properties and test results to input for finite element models is described. Simulations of the test conditions are performed to validate the inputs.

ACKNOWLEDGMENTS

We thank Howard Anderson, Lam Banh, Michael Chance, and Michael Hibbs for their assistance with procuring material and preparing test specimens. We appreciate assistance from Jhana Gearhart with uniaxial compression testing. Additionally, we thank Dave Johnson for taking micrographs of fractured specimens.

CONTENTS

FIGURES

TABLES

NOMENCLATURE

CTBN	Carboxyl Terminated Butadiene Acrylonitrile
VIDAS	VXI Data Acquisition System
DEA	Diethanolamine
DGEBA	Diglycidyl Ether of Bisphenol-A
DOE	Department of Energy
ft-lb	Foot-Pound
fps	Foot per Second
EEGMB	Epoxy-Encapsulated Glass Microballoons
GMB	Glass Microballoons
kip, kips	Thousand Pounds
ksi	Thousand Pounds per Square Inch
LDVT	Linear Variable Differential Transformer
LSTC	Livermore Software Technology Corporation
mil, mils	Thousandth Part of an Inch
MSL	Mechanical Shock Laboratory
psi	Pounds per Square Inch
sec	Second
SML	Structural Mechanics Laboratory
SNL	Sandia National Laboratories
TTL	Transistor-Transistor Logic

1. INTRODUCTION

Sensitive components are often encapsulated in syntactic foams to protect them from mechanical insults, such as the penetration of a tool. Simulations of tool impacts require material properties that encompass ultimate failure. One particular foam is evaluated to determine the appropriate material properties for a finite element model of such an impact. The syntactic foam is epoxy-encapsulated glass microballoons (EEGMB), defined by Sandia National Laboratories (SNL) material specification 9927092 (Ref. 1). The constituents are listed in Table 1.

Table 1: Constituents of 9927092 Epoxy-Encapsulated Glass Microballoons

Material	Specification	Ref.	Weight Fraction	Volume Fraction
Encapsulating Resin	2140646	2	71.4%	47.2%
Glass Microballoon Filler	6090014	3	20.0%	46.9%
Curing Agent	4604020	4	8.6%	5.9%
Total			100.0%	100.0%

The encapsulating resin is an epoxy-rubber adduct made from 90% diglycidyl ether of bisphenol-A (DGEBA, Ref. 5) and 10% carboxyl-terminated butadiene acrylonitrile (CTBN, Ref. 6) by weight. The glass microballoons (GMB) have a particle density of 0.32 grams per cubic centimeter. The volume fraction of the filler increases slightly during curing, to about 50%.

The properties of material 9927092 are summarized in Table 2. Reference 7 provides elastic and thermal properties, as well as a compressive engineering stress-strain curve at three temperatures. This report provides greater clarity on the manner of testing and the mode of failure. The modulus of elasticity in compression is determined from new test data, which are discussed in section 3.5. Poisson's ratio is taken from Reference 8. The tensile modulus of elasticity and yield stress curve are derived subsequently from data in Reference 8.

Table 2: Properties of 9927092 Epoxy-Encapsulated Glass Microballoons

Property	Symbol	Ref.	SI Unit		Customary Unit	
Density	ρ	7	770	kg/m^3	72.1E-6	$lb \cdot s^2/in^4$
Modulus of Elasticity in Tension	E		3.79E9	Pa	550E3	psi
Modulus of Elasticity in Compression	E_c		2.04E9	Pa	296E3	psi
Poisson's Ratio	ν	8	0.36		0.36	

2. TENSILE YIELD STRESS CURVE

The simulations of mechanical insults are performed with LS-DYNA version MPP D R7.1.1, an explicit dynamics program developed by Livermore Software Technology Corporation (LSTC). The 9927092 material is represented in the simulations by an isotropic constitutive model that accepts user-defined stress-strain curves for tension and compression. These curves are required to be defined in terms of true yield stress and true plastic strain (Ref. 9). The tensile engineering stress-strain curve is obtained from Reference 8, page 31, Figure 3. The curve is smoothed prior to computing the true yield stress and true plastic strain by fitting it with the fourth-order polynomial defined by Equation 1 and the coefficients in Table 3. The coefficient of determination for the fit is 0.99997. The original engineering stress-strain curve and the curve fit are plotted in Figure 1.

$$\sigma_e = a_4\varepsilon_e^4 + a_3\varepsilon_e^3 + a_2\varepsilon_e^2 + a_1\varepsilon_e + a_0 \quad (1)$$

Table 3: Coefficients for Tensile Engineering Stress-Strain Curve

Coefficient	Value
a_4	5.158E14
a_3	-1.407E13
a_2	9.146E10
a_1	2.795E9
a_0	-9.860E3

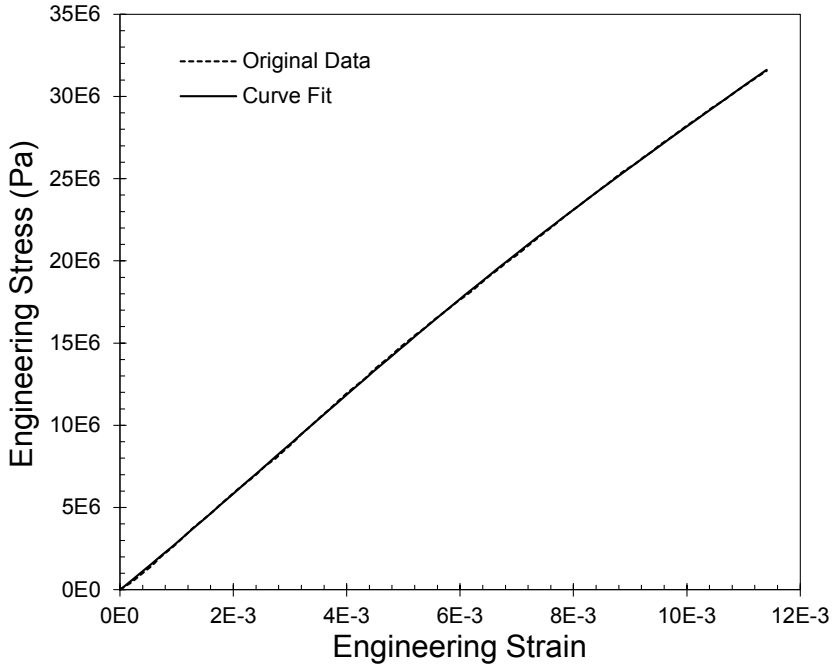

Figure 1: Tensile Stress-Strain Curve for Material 9927092

The true stress and strain are calculated with Equations 2 and 3 (Ref. 9). Equation 2 is based on an assumption of constant volume during plastic flow (Ref. 10, p. 262). Although this assumption is not true for 9927092 foam, it is useful as an approximation, and a correction factor

is applied later to compensate for it. The elastic modulus is calculated from the true stress and strain with Equation 4 and evaluates to 2.99 gigapascals; it is the maximum true secant modulus of the smoothed curve. The true plastic strain is obtained with Equation 5 (Ref. 9).

$$\sigma_t = \sigma_e(\varepsilon_e + 1) \tag{2}$$

$$\varepsilon_t = \ln(\varepsilon_e + 1) \tag{3}$$

$$E_t = \max\left(\frac{\sigma_t}{\varepsilon_t}\right) \tag{4}$$

$$\varepsilon_p = \varepsilon_t - \frac{\sigma_t}{E_t} \tag{5}$$

A one-quarter symmetric model of a one-inch-diameter cylinder is used to correlate the yield stress curve to the test data. The model is illustrated in Figure 2, and characteristics are listed in Table 4. The results are checked for convergence with the fine mesh shown in Figure 3. All of the elements in both meshes are hexahedral.

Table 4: Characteristics of Quarter-Cylinder Models for Uniaxial Tension Simulations

	Coarse	Fine
Number of Elements	244,600	1,754,800
Typical Side Length	249E-6 m 0.0098 in	127E-6 m 0.0050 in
Maximum Aspect Ratio	2.20	1.89
Minimum Taper Ratio	0.69	0.70
Maximum Skew Angle	41.8°	40.0°
Maximum Warp Angle	0.0°	0.0°
Maximum Twist Angle	8.0°	6.4°
Minimum Jacobian Ratio	0.37	0.35

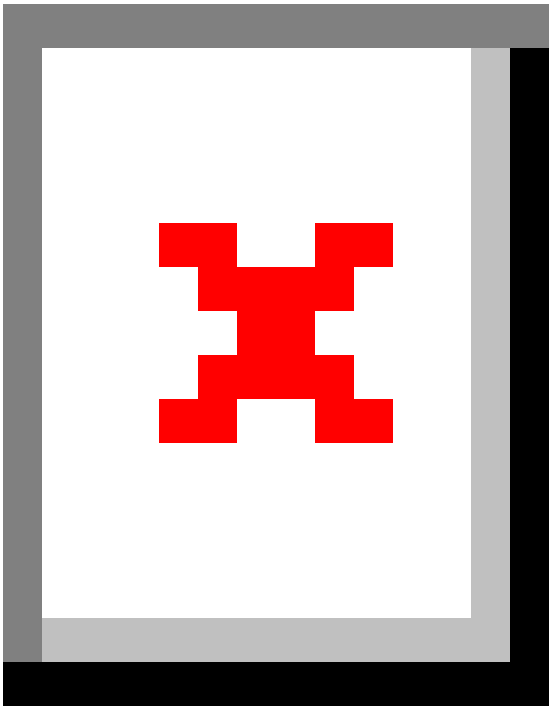

Figure 2: Coarse Model of Foam Cylinder in Tension

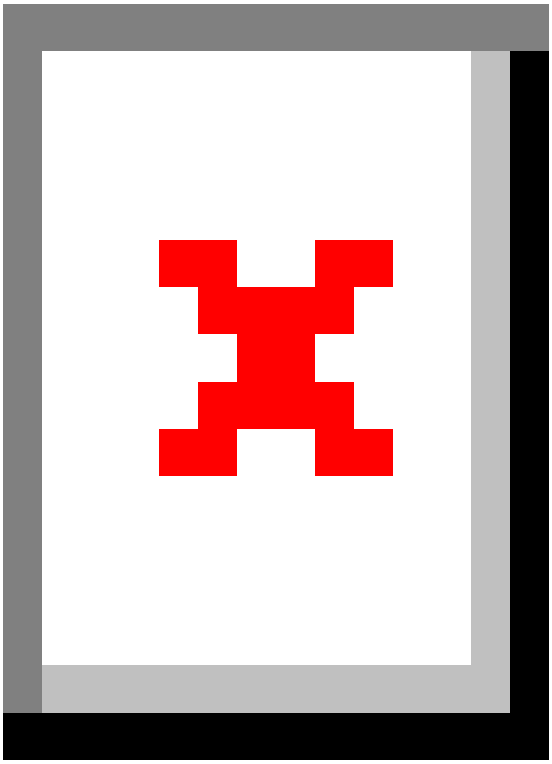

Figure 3: Fine Model of Foam Cylinder in Tension

The response of the coarse mesh in an initial simulation with the calculated yield stress curve is plotted as a dashed line in Figure 4. The engineering stress-strain curve is integrated to calculate the energy absorbed by a unit volume of the foam (the area under the stress-strain curve). The unit energy from the simulation is 21% less than the unit energy obtained from the test data. In order to linearly and uniformly raise the curve, the elastic modulus and yield curve are both scaled by a factor of 1.267. The scaled elastic modulus is 3.79 gigapascals, and the yield stress curve is plotted in Figure 5; the true stress is defined by Equation 2, and the true plastic strain is defined by Equation 5. The result is the correlated simulation in Figure 4; the maximum stress of the correlated simulation differs from the test data by 0.02%, and the unit energy differs from that of the original stress-strain curve by 0.01%. The convergence check is performed with the fine mesh and the scaled inputs and corroborates the results of the correlated simulation. The relative difference in the maximum stress calculated by the coarse and fine models is 0.004%; the relative difference in the unit energy is 0.002%.

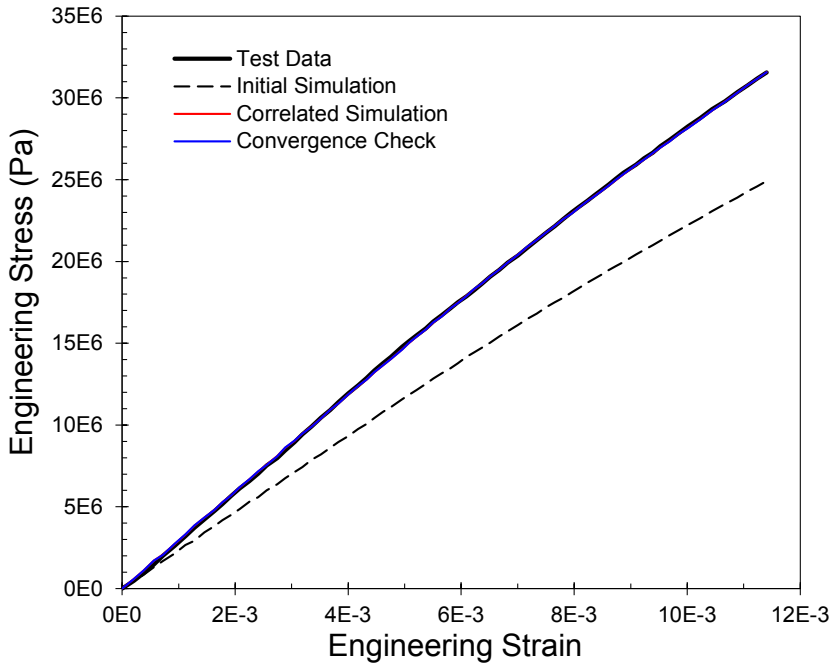

Figure 4: Correlation of Tensile Stress-Strain Curve to Test Data

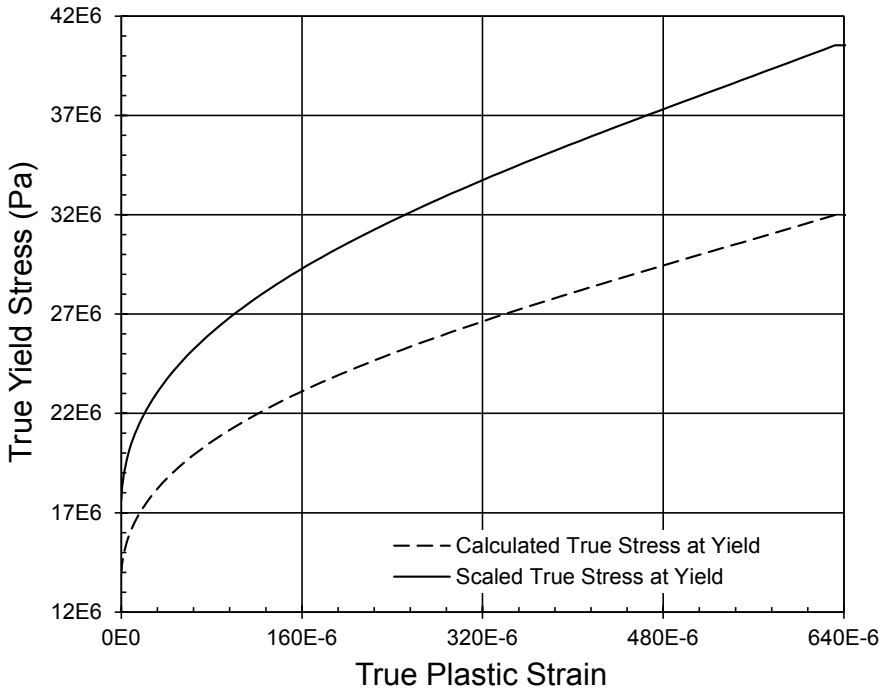

Figure 5: Tensile Yield Stress Curve for Material 9927092

The maximum engineering strain in Reference 8 is 0.0114. If the elements in the coarse mesh of Figure 3 are eroded at a maximum shear strain of 0.0078, the quarter cylinder breaks at an engineering strain of 0.0115, which is 0.4% greater than the failure strain in the test data.

3. COMPRESSIVE YIELD STRESS CURVE

3.1. Compression Sample Preparation

The uniaxial compression samples were prepared per Reference 1 from new material, poured in cylindrical tubes with a nominal diameter of one inch. The cure process began in a vacuum chamber to prevent the formation of gas bubbles. The cured cylinders were cut on a machine lathe to form samples with a nominal height of one inch. The break-away point at the center axis was manually polished to smooth the surface. The height of each sample was measured with a micrometer caliper; the diameter was measured in two orthogonal directions and averaged. The mean diameter and 99% precision interval is 26.50±0.169 millimeters; the mean height and 99% precision interval is 25.37±0.278 millimeters. In processing the test data, the dimensions of each sample (rather than the mean values) were used to calculate the stress and strain for that sample.

3.2. Uniaxial Compression Test Method

Twelve uniaxial compression tests of 9927092 syntactic foam were performed in the Structural Mechanics Laboratory (SML) to determine the quasi-static stress-strain curve. The tests were conducted between 27 and 28 July 2015. The cylindrical samples were uniaxially compressed to a displacement of 0.8 inches. Data acquired during the tests included load and actuator stroke.

The foam samples were placed between platens in a 22-kip load test frame as shown in Figure 6. The platens were measured and adjusted for parallelism to prevent premature failure and were found to be parallel within 0.5 mils. Force was measured using the 22-kip load cell on the test frame. Displacement was measured using the test frame actuator Linear Variable Differential Transformer (LVDT). Video was recorded of each test. In order to show the load in the video, a voltmeter was placed in the field of view of the video camera. The voltmeter was set up such that one volt was equivalent to a load of one kip.

Prior to testing the samples were measured and marked with the letters A through M for identification and a color pattern to facilitate reconstruction of the fragments. The samples were tested in reverse alphabetical order. Sample A was not tested because the first 12 samples produced consistent results. The first sample tested (Sample M) was compressed at a rate of 0.5 mil per second. Subsequent samples (Samples L through B) were compressed at a rate of 0.5 mils per second for the first 0.1 inches of compression, 1.0 mil per second until the sample was compressed 0.2 inches, and 2 mils per second for the remainder of the test. Table 5 provides a summary of the sensors used for testing and the calibration date associated with each sensor. During testing, clear tape was placed around the lower platen in order to facilitate collection of each sample at the conclusion of each test.

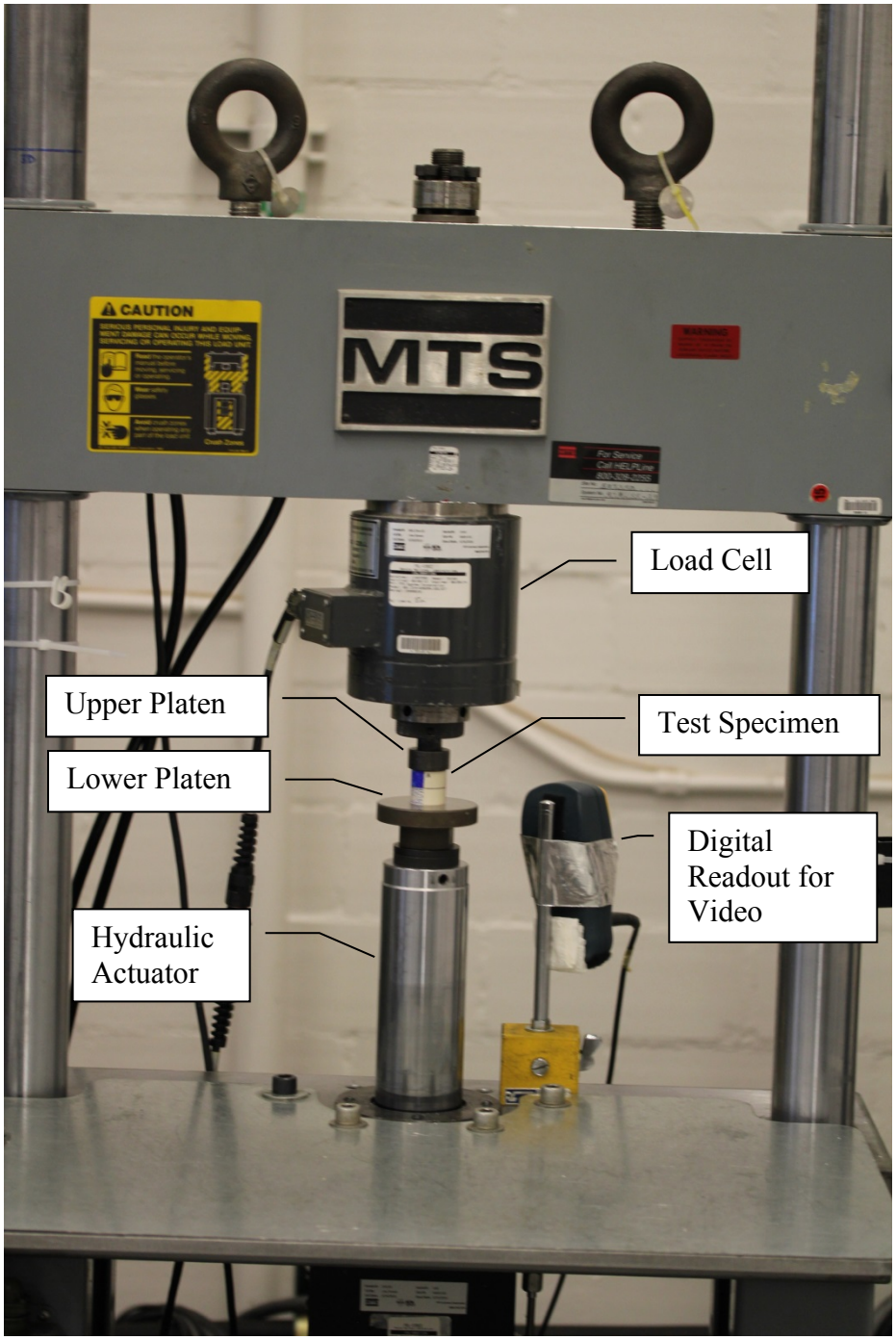

Figure 6: Test Setup

Table 5: Instrumentation for Compressing Syntactic Foam Cylinders

Sensor	Sensor Type	Model Number	Serial Number	Calibration Expiration Date
22-kip Load Cell	Force	661.21A-03	1545	06/16/2016
Actuator Stroke LVDT	Displacement	204.63	518	06/15/2016
Micrometer	Length	Mitutoyo	35071774	06/04/2016

3.3. Results of Uniaxial Compression Tests

The observed mode of failure in all of the samples is the formation of a crack from the bottom surface to a point on the opposite vertical side, as shown below. The color pattern on the sample facilitates observing the failure and reconstructing the fragments. The angle from the bottom surface to the crack face is approximately 45 degrees in most of the samples. This indicates that failure is likely to be predicted by a maximum shear stress criterion.

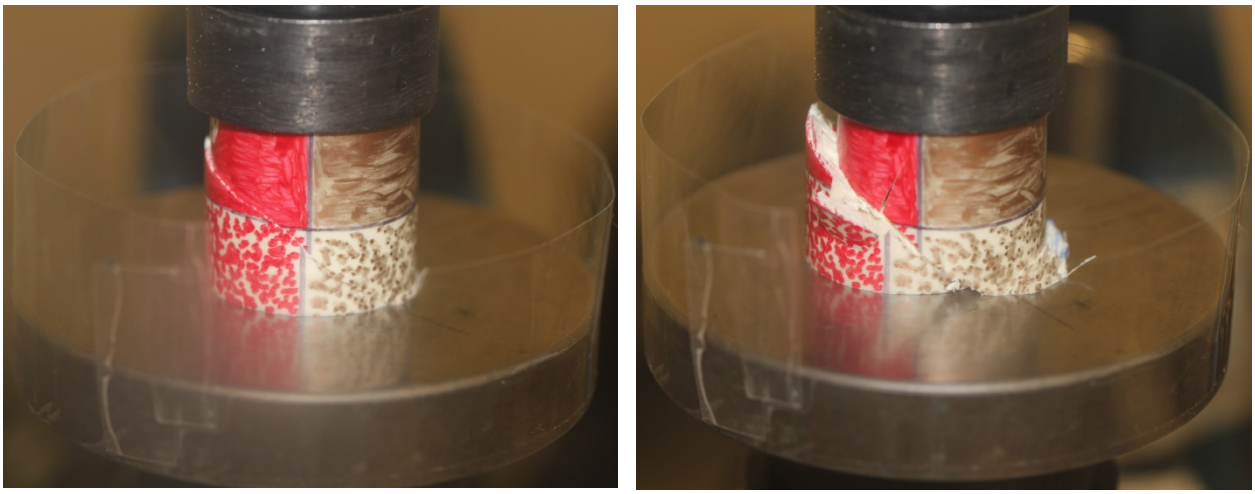

Figure 7: Sample G Displays Typical Failure Mode

After the initial failure, the foam continued to fracture into smaller pieces at random times. The samples all failed in a brittle manner, initially fracturing along a diagonal plane, an example of which is shown at the right-hand side of Figure 8.

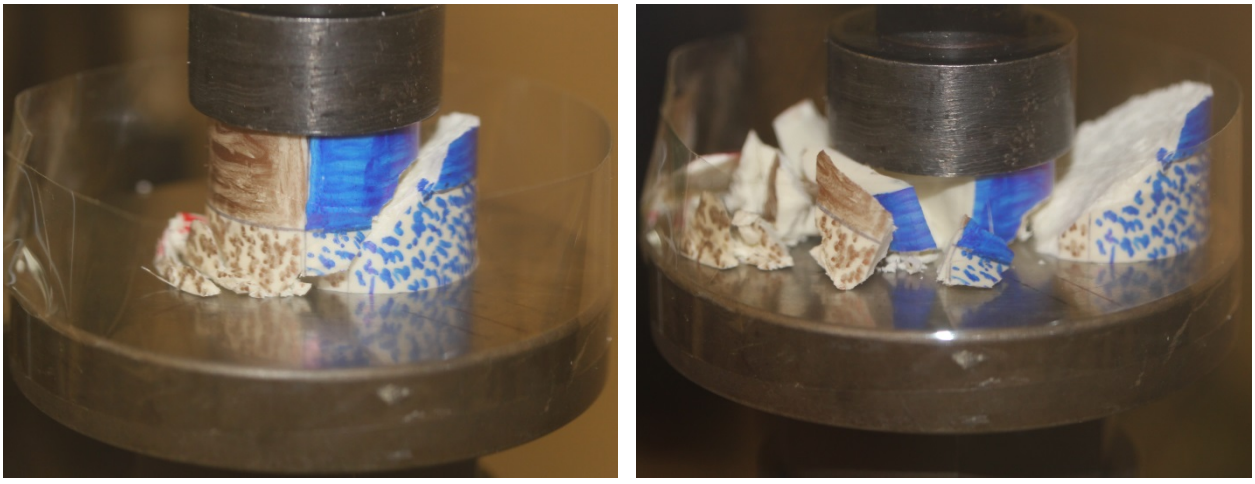

Figure 8: Sample H Fractures During Testing

The 45 degree crack face of Sample D was examined using optical microscopy as seen in Figure 9. The micrograph shows clear evidence of broken glass microballoons.

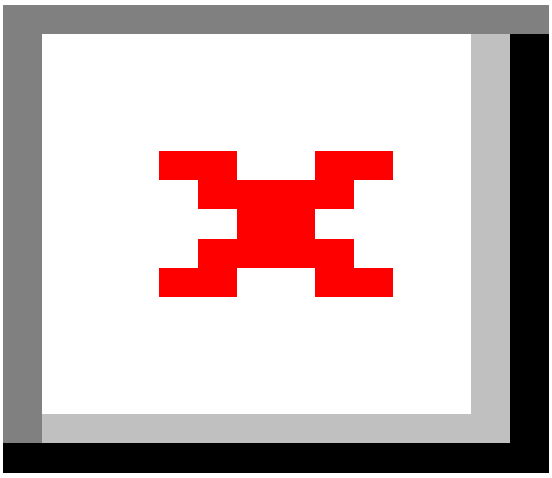

Figure 9: Magnified View of Sample D Fracture Surface

A plot of force versus displacement is given in Figure 10 while Figure 11 zooms in on the first peak in the data (i.e. the initial failure portion of the data). Displacement is shown on the abscissa in units of millimeters and force is shown on the ordinate in kilonewtons. Note that the displacement values were shifted along the abscissa so that the linear portions of the loading curves were aligned in order to facilitate comparison of sample-to-sample variation during that portion of the loading cycle. A sign convention was chosen such that force and displacement are given in positive units. The samples behaved in a very consistent manner until failure occurred, as evidenced by the data in Figures 10 and 11.

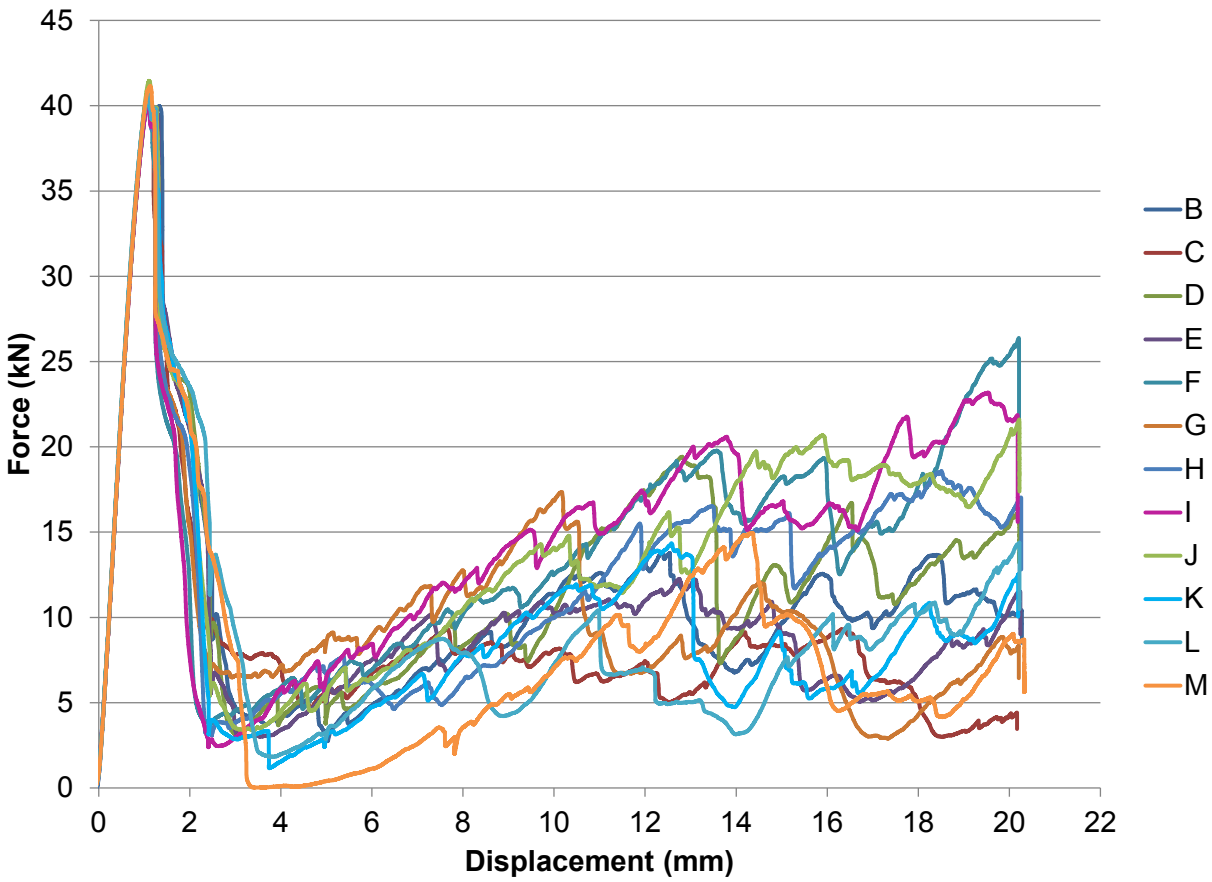

Figure 10: Force *vs.* Displacement for All Samples

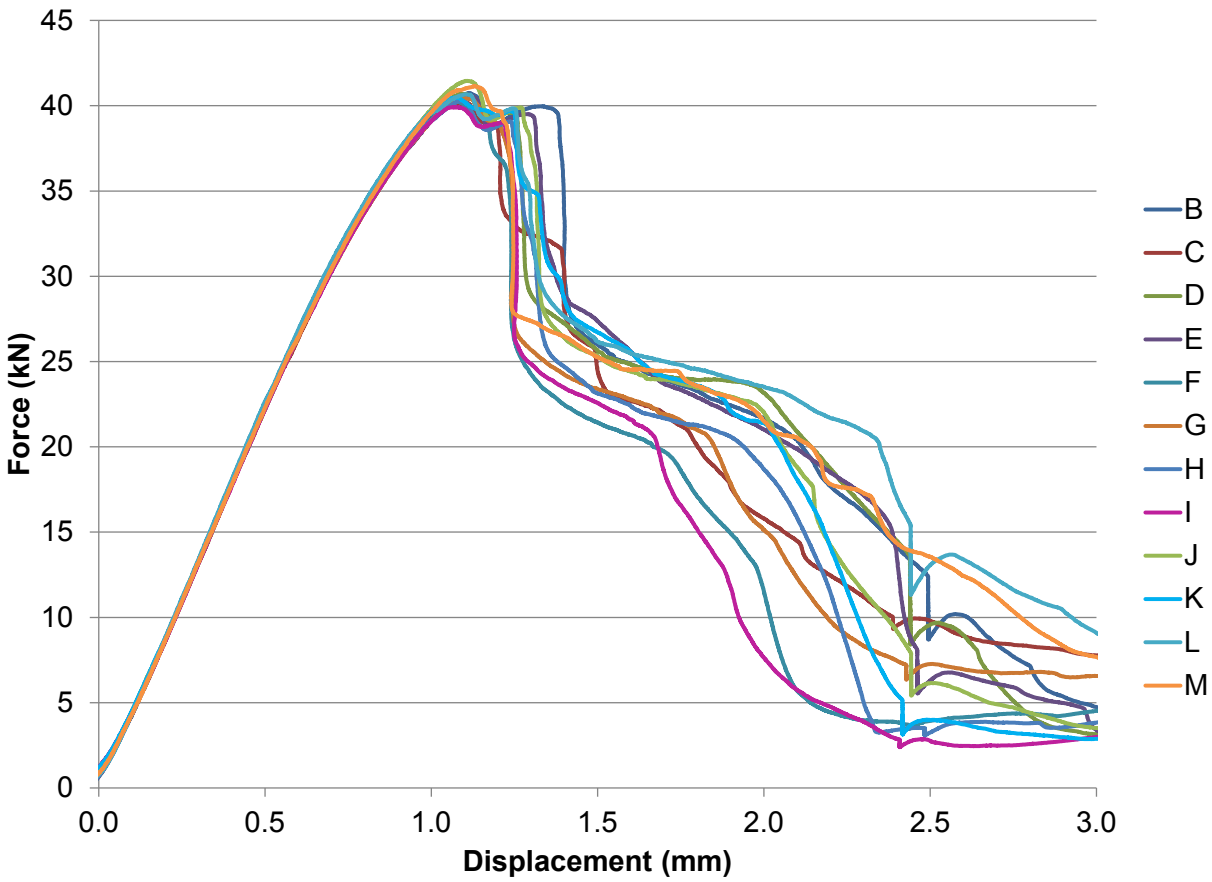

Figure 11: Detail of Force *vs.* Displacement Showing Initial Failure Portion of Data

The peak stress and modulus of elasticity were calculated with the cross-sectional area based on the average diameter of the individual sample. The modulus of elasticity was taken as the slope of stress versus strain over the approximately linear portion of the curve (for stress between 14 and 55 megapascals, Fig. 14). The calculated peak stress and modulus of elasticity are given for each sample in Table 6 as well as averages and standard deviations. Note that the plots in Figures 10 and 11 as well as the calculated values for stress and modulus of elasticity represent raw data (i.e. the compliance was not subtracted out).

Table 6: Summary of Peak Stress and Modulus of Elasticity

	Peak Stress		Modulus of Elasticity	
Sample	MPa	ksi	GPa	ksi
B	73.4	10.64	2.01	292
C	72.9	10.58	2.02	294
D	73.7	10.69	2.04	295
E	73.8	10.71	2.03	294
F	72.8	10.56	2.03	294
G	73.4	10.65	2.04	295
H	73.2	10.62	2.03	294
I	72.3	10.49	2.03	294
J	75.4	10.93	2.06	298
K	73.6	10.67	2.06	299
L	73.4	10.64	2.03	295
M	75.2	10.91	2.06	298
Average	73.6	10.67	2.04	295
Standard Deviation	0.9	0.13	0.01	2

3.4. Uncertainty in Compression Tests

One source of uncertainty in material testing is the compliance of the test machine. The compliance was measured by compressing a steel cylinder with an average diameter of 25.38 millimeters (from two orthogonal measurements) and a height of 25.36 millimeters (nominally the same dimensions as the foam samples). The steel cylinder was compressed to a maximum force of 44.6 kilonewtons. The force-displacement data are plotted in Figure 12. The LVDT registered less displacement at a given force while the force was increasing and greater displacement while the force was decreasing. The meaningful test data are collected as the force on a foam sample is increasing, so only the compliance data for increasing load were considered. The compliance curve is the difference between the force-displacement curve of the steel sample and the theoretical linear elastic response; it is plotted in Figure 13. The maximum principal stress in the steel cylinder was 88.1 megapascals, which is well below the yield strength of mild steel (248 megapascals, Ref. 11, p. 2-8, Table 2.2.1.0(b), AISI 1025 bar). A polynomial fit to the compliance curve provides a single value of displacement for a given force. It is plotted as a dashed line in Figure 13 and has a coefficient of determination of 0.9995. The displacement due to compliance is calculated from the measured force at each data point in the foam tests and is subtracted from the measured displacement. The effect is a slight straightening of the force-displacement curve for forces below 10 kilonewtons.

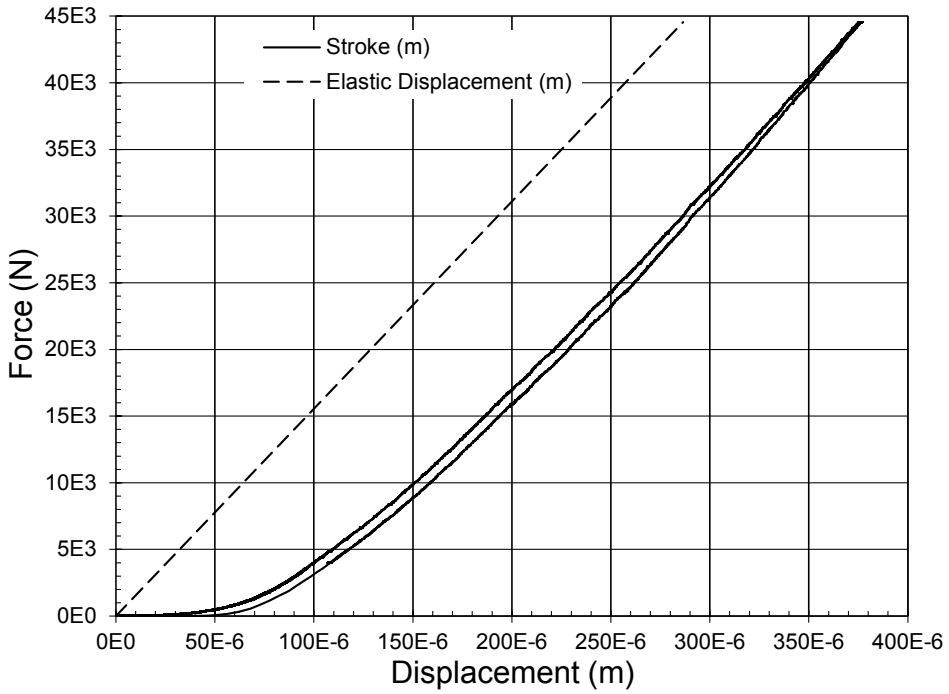

Figure 12: Uniaxial Compression Test of a Steel Cylinder and Theoretical Elastic Response

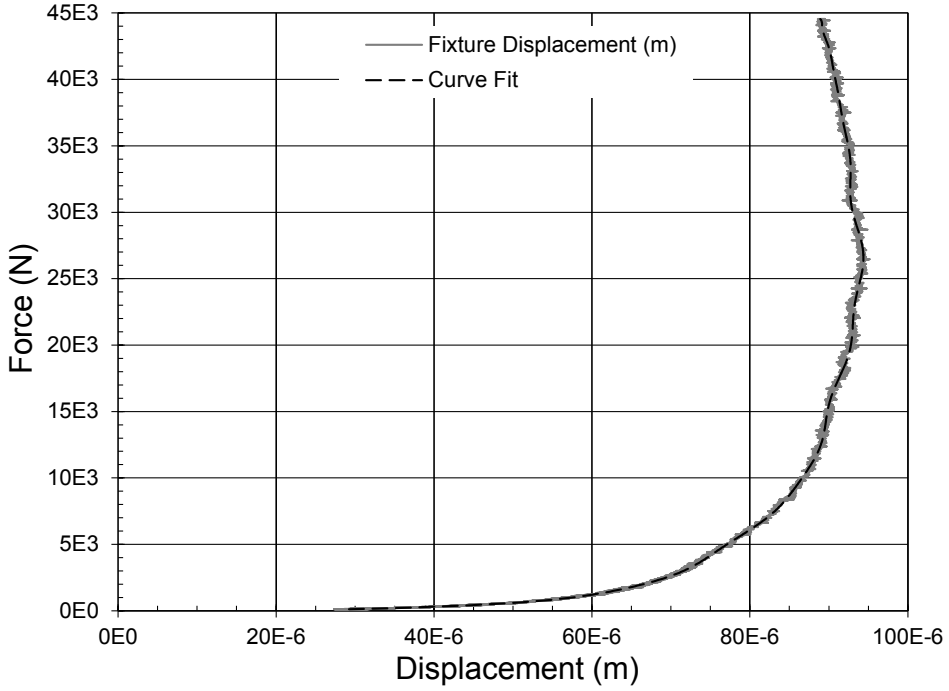

Figure 13: Compliance Curve for Increasing Load and Curve Fit

In addition to compliance, there is uncertainty in locating the origin of each force-displacement curve. The load cell reads a low level of force when unloaded (although it is calibrated to read accurately over its useful range), and there are imperfections in the samples that cause them to load up gradually. The most consistent portion of the force-displacement curve is the linear elastic region between 20 and 40 megapascals. A straight line is fit to the linear elastic portion of the curve for each test, and the intersection of this line with the zero-force axis defines the origin of the curve. The displacement data are shifted such that the origin is at zero displacement and

the linear portions of the curves are aligned. The engineering stress and strain are calculated from the original force data, the shifted displacements with compliance removed, and the actual sample dimensions. The stress-strain curve for each of the twelve samples is plotted in Figure 14. The mean stress-strain curve is shown in Figure 15 with a precision interval based on 99% probability.

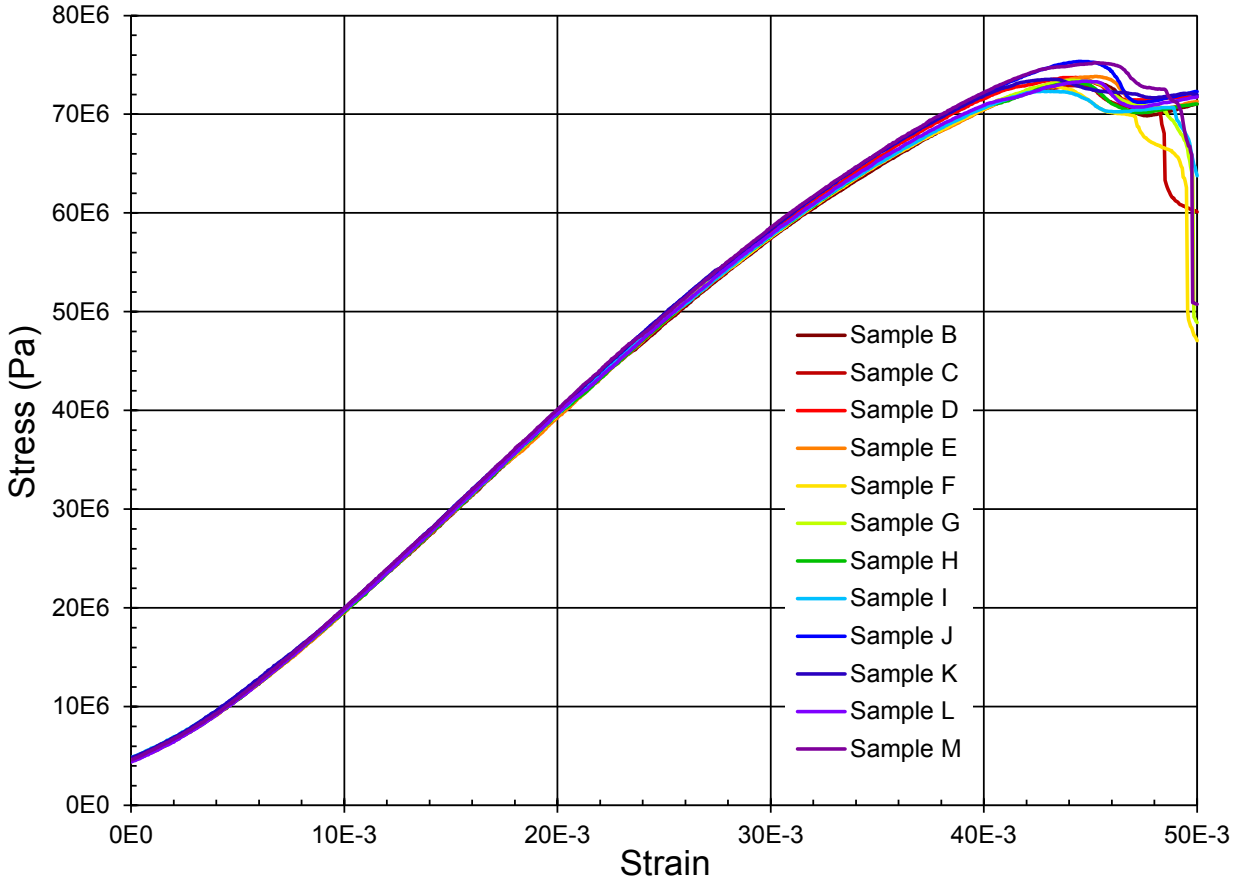

Figure 14: Uniaxial Compression Test Results for 9927092

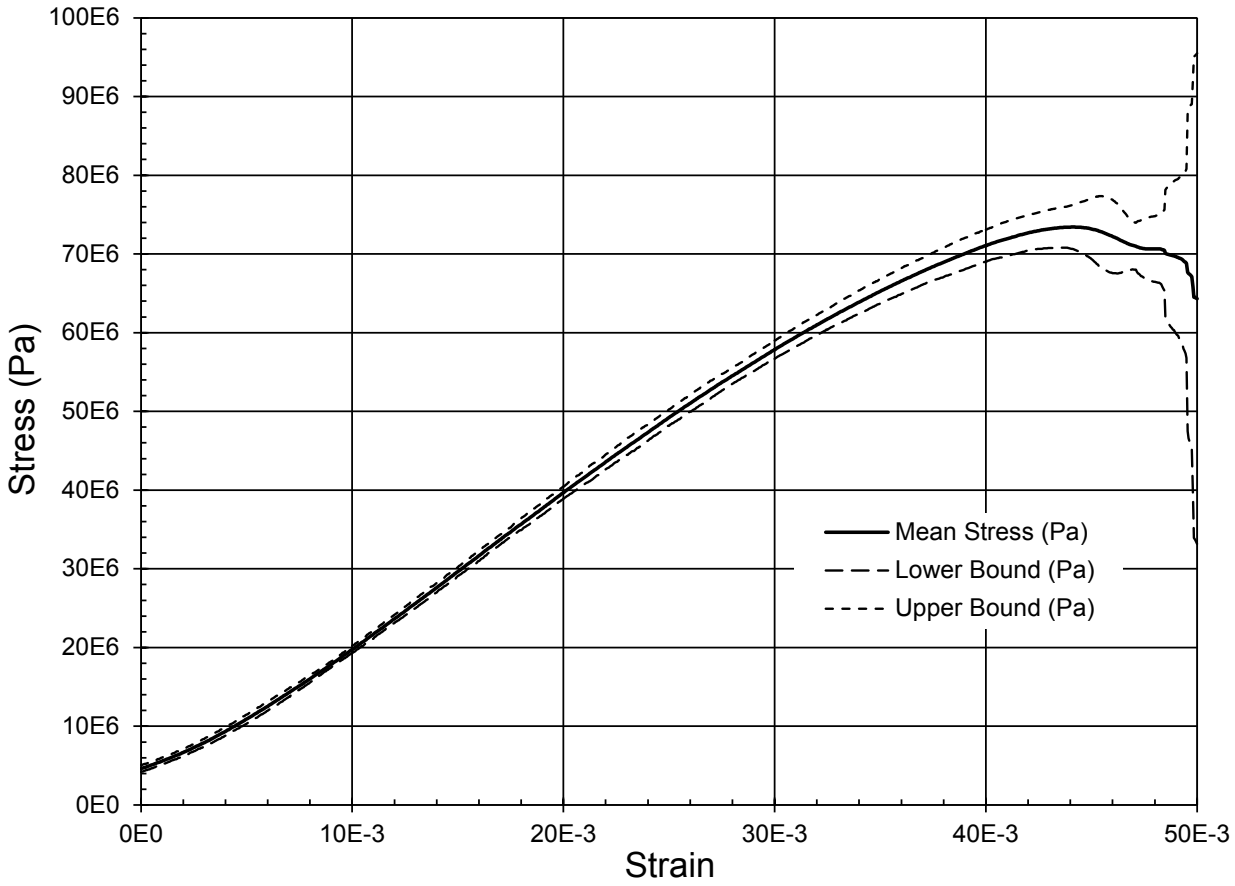

Figure 15: Mean Compressive Stress-Strain Curve and 99% Precision Interval

A third form of uncertainty that is present in material testing is the variability in material properties that results from manufacturing processes and aging. Although the samples were prepared in accordance with the instructions in specification 9927092, variations in the mixing and curing times and temperatures are allowed within certain limits, and variations in strength result. Furthermore, the samples are not artificially aged, so they may have greater toughness than material that has been in service for several years. This affects the applicability of the derived material properties to components that have been encapsulated in 9927092 foam.

3.5. Compressive Stress-Strain Curve

The mean stress-strain curve is trimmed at low strain to follow the secant modulus up to 20 millistrain, where it intersects the curve. The failure strain is identified at the point of inflection after the maximum stress and corresponds to the formation of a crack through the sample.

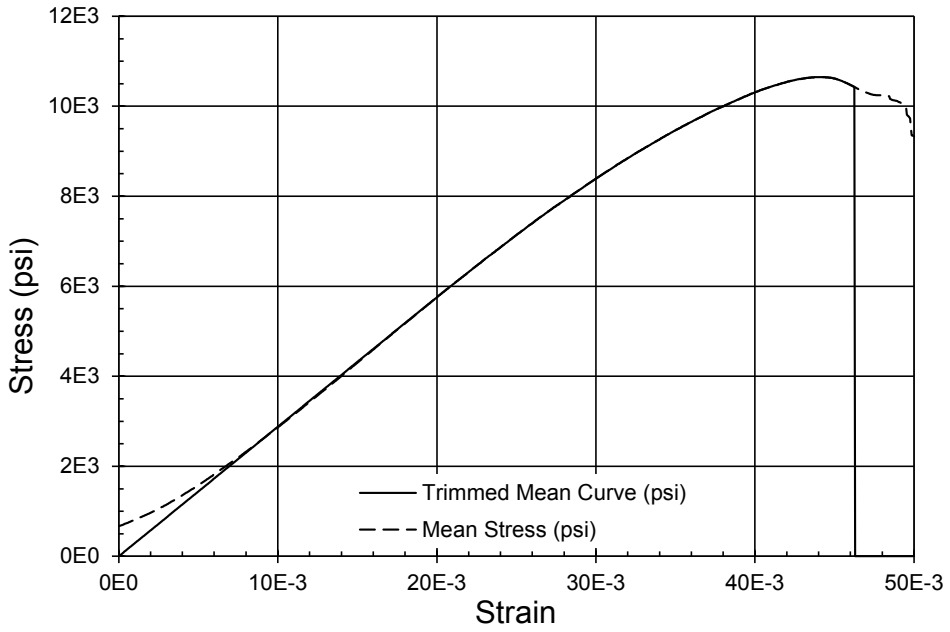

Figure 16: Mean Compressive Stress-Strain Curve and Trimmed Curve

The trimmed curve is smoothed prior to computing the true yield stress and true plastic strain by fitting it with the ninth-order polynomial defined by Equations 6 and 7 and the coefficients in Table 7. This eliminates noise that would be amplified by the conversion to plastic strain, resulting in smooth input for the material model. The coefficient of determination for the fit is 0.9999992. The original engineering stress-strain curve and the curve fit are plotted in Figure 17.

$$\hat{\varepsilon}_e = \frac{\varepsilon_e - \mu_\varepsilon}{\sigma_\varepsilon} \tag{6}$$

$$\sigma_e = a_9\hat{\varepsilon}_e^9 + a_8\hat{\varepsilon}_e^8 + a_7\hat{\varepsilon}_e^7 + a_6\hat{\varepsilon}_e^6 + a_5\hat{\varepsilon}_e^5 + a_4\hat{\varepsilon}_e^4 + a_3\hat{\varepsilon}_e^3 + a_2\hat{\varepsilon}_e^2 + a_1\hat{\varepsilon}_e + a_0 \tag{7}$$

Table 7: Coefficients for Compressive Engineering Stress-Strain Curve

Coefficient	Value
a_9	-1.434E5
a_8	9.167E5
a_7	-2.075E6
a_6	1.461E6
a_5	1.464E6
a_4	-2.694E6
a_3	-8.366E5
a_2	5.021E5
a_1	3.045E7
a_0	2.252E7
μ_ε	1.059E-2
σ_ε	1.427E-2

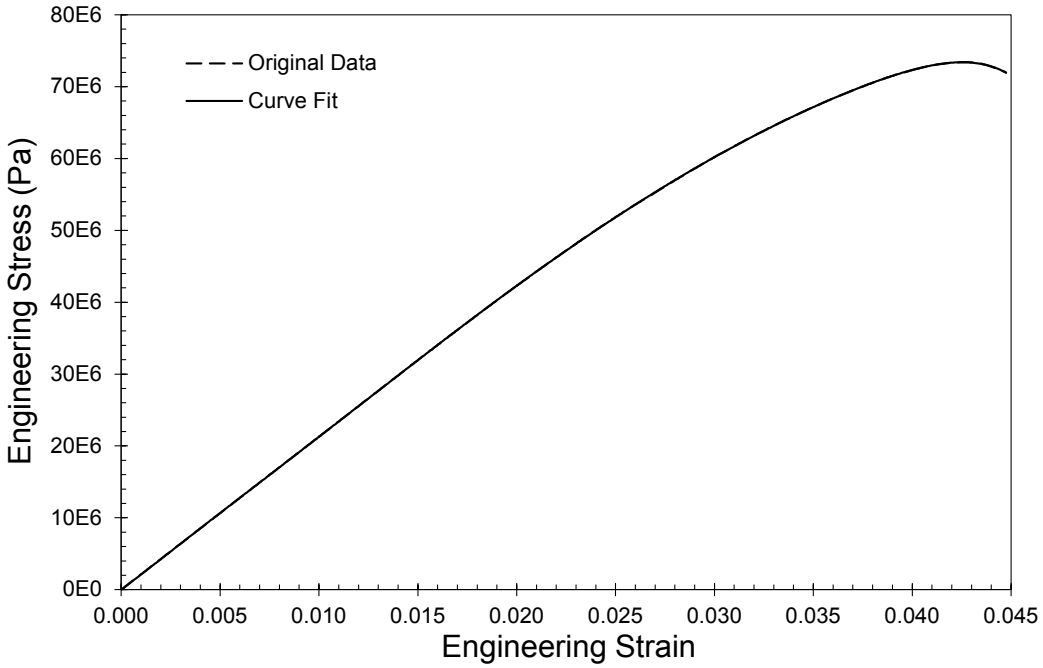

Figure 17: Compressive Engineering Stress-Strain Curve for Material 9927092

3.6. Correlated Material Model

The true stress and true plastic strain are calculated with Equations 2 and 5 (page 4). The elastic modulus is taken as the maximum true secant modulus of the stress-strain data and evaluates to 2.18 gigapascals (Eq. 4). A one-quarter symmetric model of a one-inch-diameter cylinder is used to correlate the yield stress curve to these data. The model is illustrated in Figure 18, and characteristics are listed in Table 8. The results are checked for convergence with the fine mesh shown in Figure 19. All of the elements representing the foam are hexahedral. Shell elements function as platens to compress the foam and as barriers at the symmetry plate. Beam elements measure the force and form a rigid body attached to the moving platen so that it can be guided with one degree of freedom. The complete model is displayed in Figure 20; only the foam and platens are displayed in Figures 18 and 19.

Table 8: Characteristics of Quarter-Cylinder Models for Uniaxial Compression Simulations

	Coarse	Fine
Number of Elements	244,609	1,754,809
Typical Side Length	249E-6 m 0.0098 in	127E-6 m 0.0050 in
Maximum Aspect Ratio	2.20	1.89
Minimum Taper Ratio	0.69	0.70
Maximum Skew Angle	41.8°	40.0°
Maximum Warp Angle	0.0°	0.0°
Maximum Twist Angle	8.0°	6.4°
Minimum Jacobian Ratio	0.37	0.35

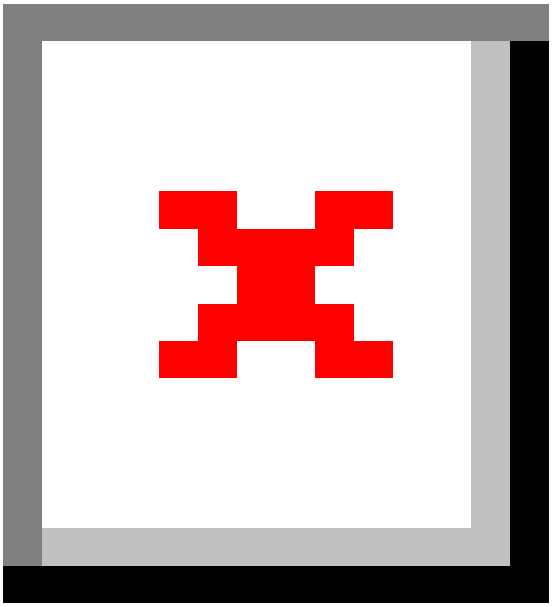

Figure 18: Coarse Model of Foam Cylinder in Compression

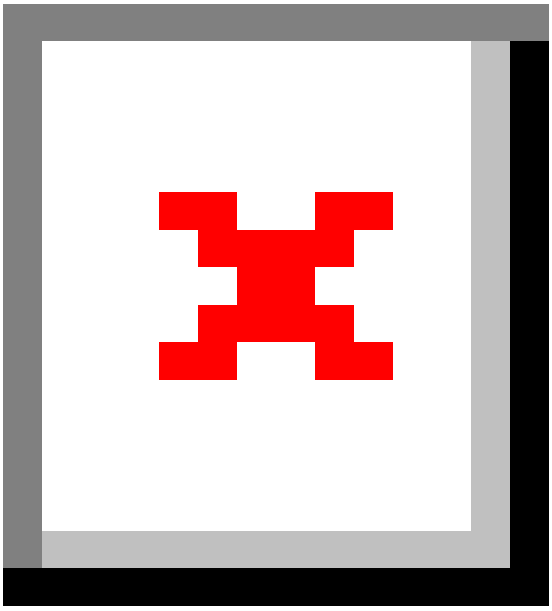

Figure 19: Fine Model of Foam Cylinder in Compression

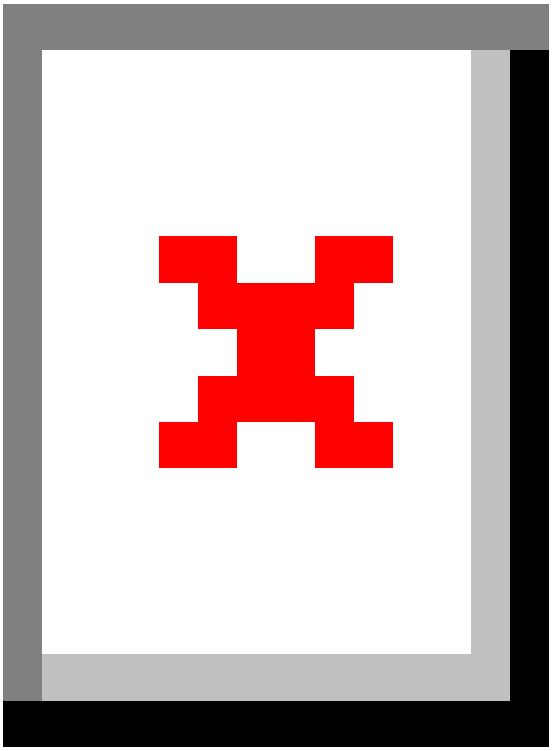

Figure 20: Complete Model of Foam Cylinder in Compression

The engineering stress-strain curve resulting from the initial simulation with the coarse mesh and the calculated yield stress curve is plotted as a dashed line in Figure 21. The engineering stress-strain curve is 7.4% greater than the test data; in order to linearly and uniformly lower the curve, the elastic modulus and yield curve are both scaled by a factor of 0.930. The scaled elastic modulus is 2.04 gigapascals, and the yield stress curve is plotted in Figure 22; the true stress is defined by Equation 2, and the true plastic strain is defined by Equation 5 (page 4). The result is

a correlated material model, which was used as input for the final simulation. The engineering stress-strain curve resulting from the final simulation with the correlated material model is plotted as a red line in Figure 21; the maximum stress differs from the test data by 0.39%, and the unit energy (area under the stress-strain curve) differs by 0.02%. The convergence check is performed with the fine mesh and the correlated material model; it corroborates the results of the final simulation. The relative difference in the maximum stress calculated by the coarse and fine models is 0.05%; the relative difference in the unit energy is 1.2%.

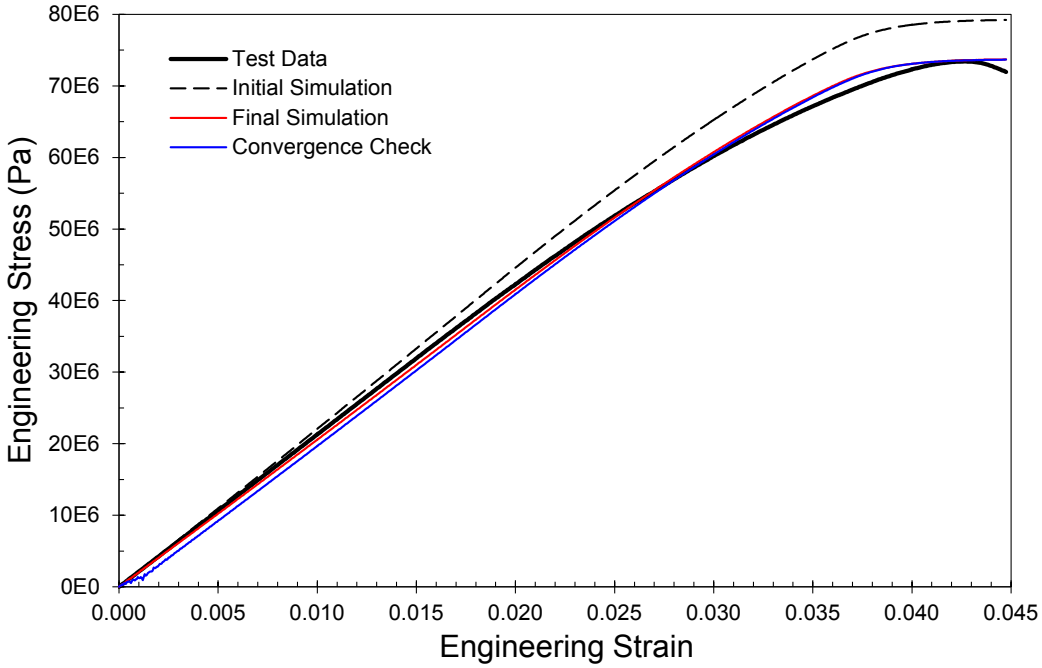

Figure 21: Correlation of Compressive Stress-Strain Curve to Test Data

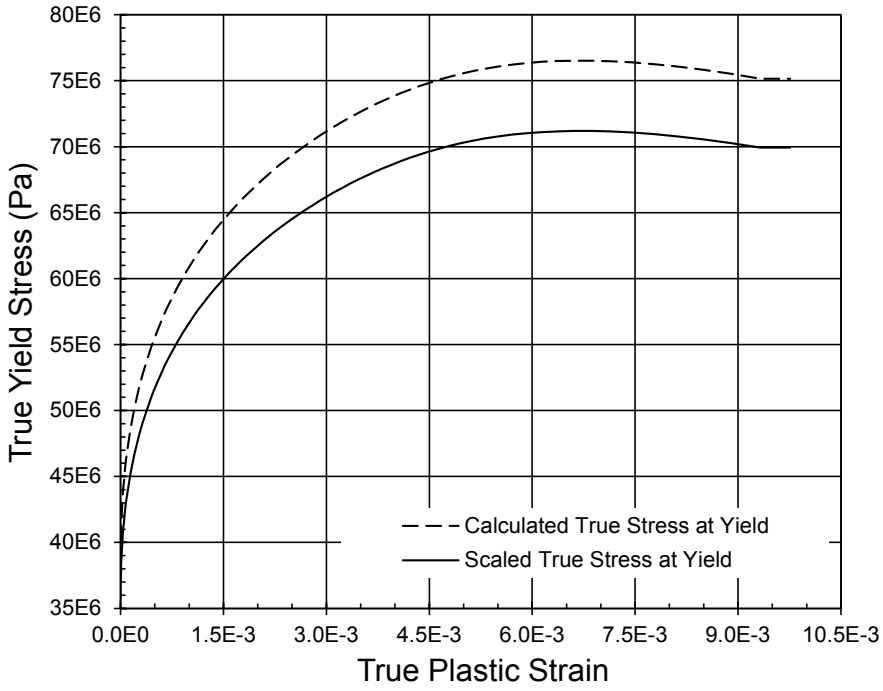

Figure 22: Compressive Yield Stress Curve for Material 9927092

The maximum engineering strain in Figure 17 is 0.0448. If the elements in the coarse mesh of Figure 18 are eroded at a maximum shear strain of 0.0543, the quarter cylinder breaks at an engineering strain of 0.0448, 0.2% greater than the failure strain calculated from the test data.

4. FAILURE MODEL DEVELOPMENT

4.1. Impact Sample Preparation

Ten rectangular prismatic blocks of 9927092 foam were cast from new material in batches of two. The material for the samples was prepared per Reference 1. The molds were machined from aluminum to control the length of 5 inches and the width of 2 inches. The samples were poured to a nominal depth of 5 inches, placed under vacuum to remove gas bubbles, and cured. A final machining operation removed sharp edges and refined the dimension in the pour depth direction.

4.2. Probe Impact Test Method

Probe penetration tests were conducted in the Mechanical Shock Lab (MSL) on 29 July 2015 to quantify the energy absorbed by material 9927092. The 10 samples were subjected to impact tests on a modified drop table equipped with a cylindrical steel probe. Laser sensors and accelerometers were used to measure the position and velocity of the drop table carriage before and after impact, and based on the position and velocity measurements, the energy required to puncture the sample was calculated.

All tests were conducted on a modified drop table located in the MSL. Unlike a traditional drop table test where a component is mounted to the top of the drop table carriage and subjected to a haversine-shaped shock pulse, in this test series the syntactic foam samples were placed on a fixture assembly on top of the drop table reaction mass. A cylindrical probe was mounted to the bottom of the carriage, and when the carriage was dropped, the probe impacted the foam sample. The probe consisted of a one-quarter-inch-diameter steel cylinder approximately 2.75 inches long; behind the cylindrical portion, the probe flared out in a conical shape to a maximum diameter of approximately 4 inches. The leading surface of the probe was flat. The total weight of the carriage and probe was 307 pounds. A stack of felt and steel rings was placed on top of the reaction mass fixture assembly to stop motion of the carriage after impact. In order to examine the response of the foam to the cylindrical portion of the probe, the height of the felt and steel stack was chosen to stop the carriage after the cylindrical portion of the probe completely penetrated the sample but before the conical portion reached it. The blocks were supported beneath by a steel plate with a 1.25-inch-diameter opening for the probe to pass through. The samples were attached to the plate with tape for a soft restraint. The test setup is shown in Figures 23 and 24. The majority of the felt and steel rings have been removed in these figures to allow the probe and sample to be seen.

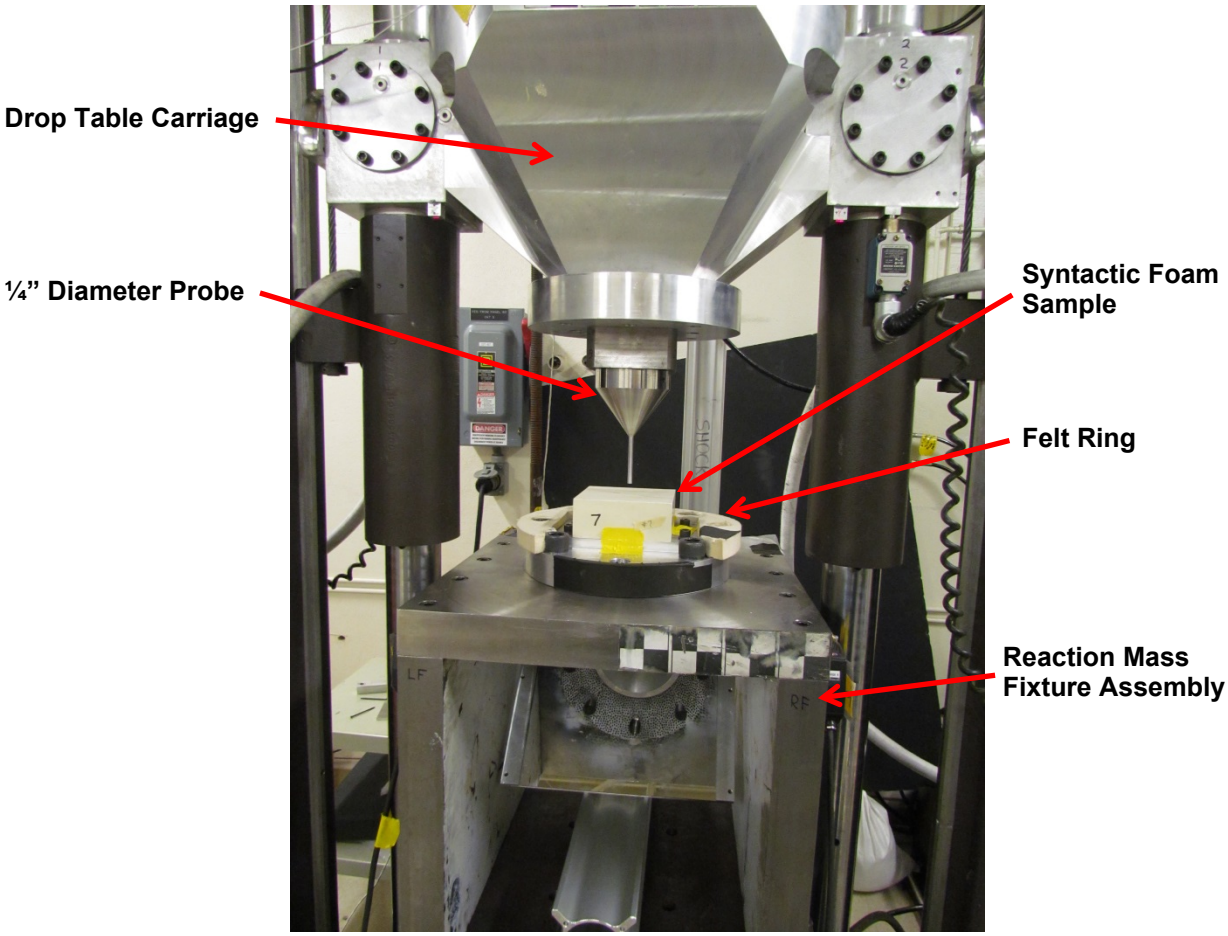

Figure 23: Drop Table Test Setup

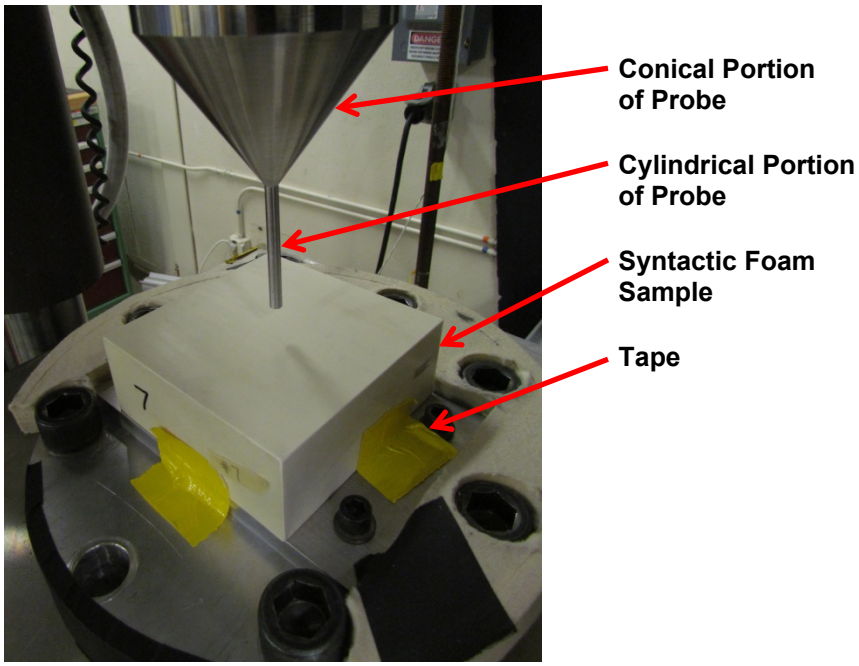

Figure 24: Close View of Probe and Foam Sample

Accelerometers, displacement lasers, and a high-speed video camera were used to capture data during the foam impact tests. Two Endevco 7270A accelerometers were mounted to the top of the drop table carriage and measured the acceleration level on the carriage throughout the tests. Two Keyence displacement lasers with a ±100-millimeter measurement range tracked the position of the drop table carriage during the tests. The lasers measured the location of the left and right side of the carriage, and the average of the two readings was used for subsequent velocity and energy calculations. A Phantom camera from Vision Research was used to capture high-speed video (approximately 6,000 frames per second) of the underside of the foam sample during each test. Due to space constraints and the potential for equipment damage, the camera could not be mounted directly beneath the test sample. Instead, the camera was placed in front of the drop table and a mirror angled at 45 degrees provided a view of the underside of the sample. Figure 25 shows the location of the instrumentation used during the tests.

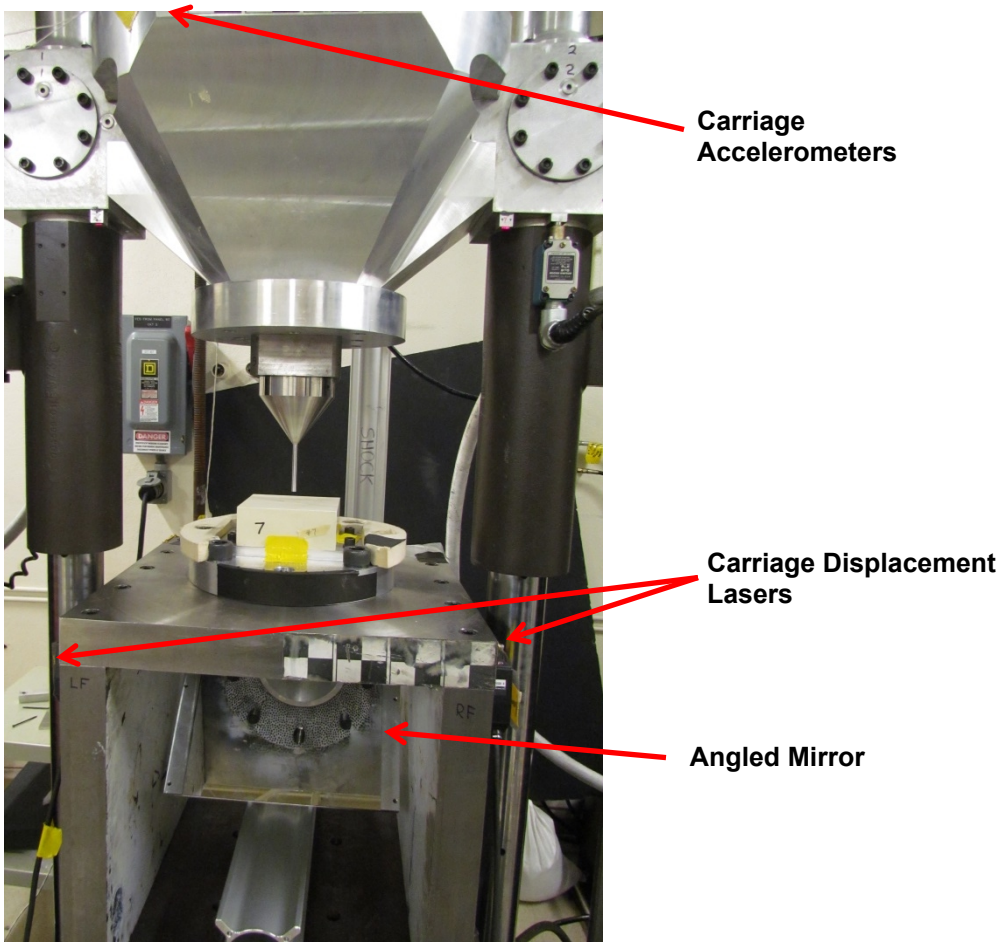

Figure 25: Foam Impact Test Instrumentation Locations

A Spectral Dynamics VXI Data Acquisition System (VIDAS) was used to capture the data from the accelerometers and displacement lasers. The VIDAS system acquired data at a rate of 2.5 megahertz, and after capture, the signals from all sensors were carefully examined for any signs of sensor problems or failures. The VIDAS system was triggered by a knife edge sensor mounted on the drop table carriage, and a Transistor-Transistor Logic (TTL) output signal from the VIDAS system was used to trigger the high-speed camera and synchronize the time base of the high-speed video with the VIDAS system.

4.3. Results of Probe Impact Tests

Impact tests were conducted on a total of 10 syntactic foam samples. The position values from the lasers were used to calculate the carriage velocity during each test. Based on the position and velocity data, the kinetic energy, potential energy, and total energy of the carriage were calculated. In an ideal system, the total energy of the carriage would remain constant up until the point of impact with the foam sample. However, the calculated total energy decreased during the course of each test due to friction between the drop table carriage and guide rods. The effects of the friction losses were removed by adjusting the gravitational acceleration to 6.5 meters per second squared in the potential energy calculation such that the total energy of the carriage remained constant while it was in free-fall. Both the kinetic and potential energy values were calculated using a carriage mass of 139.3 kilograms and the potential energy of the carriage was defined to be zero at the point of initial impact with the felt and steel stop rings.

Of the 10 samples tested, five were completely punctured by the test probe, whereas, in the other five tests, the probe only partially penetrated the sample. Table 9 summarizes the conditions and results of each test.

Table 9: Syntactic Foam Test Conditions and Results

Sample Number	Test Number	Drop Height (mm)	Drop Height (in)	Impact Velocity (m/s)	Impact Velocity (fps)	Test Results
1	4	152	6.00	1.32	4.3	Probe did not fully penetrate sample
2	5	406	16.00	1.90	6.2	Sample split into two pieces
3	6	203	8.00	1.56	5.1	Sample split into two pieces
4	7	178	7.00	1.45	4.8	Sample split into two pieces
5	8	165	6.50	1.38	4.5	Sample split into two pieces
6	9	152	6.00	1.31	4.3	Probe did not fully penetrate sample
7	10	159	6.25	1.35	4.4	Sample split into two pieces
8	11	156	6.13	1.31	4.3	Probe did not fully penetrate sample
9	12	159	6.25	1.33	4.4	Probe did not fully penetrate sample
10	13	165	6.50	1.35	4.4	Probe did not fully penetrate sample

The plots in Figures 26 and 27 show the velocity and energy data captured during a test where the probe only partially penetrated the sample. Figures 28 and 29 plot the velocity and energy for a test in which the probe fully penetrated the sample. The discontinuity in the data at about 10 milliseconds represents the point at which the displacement lasers started returning data.

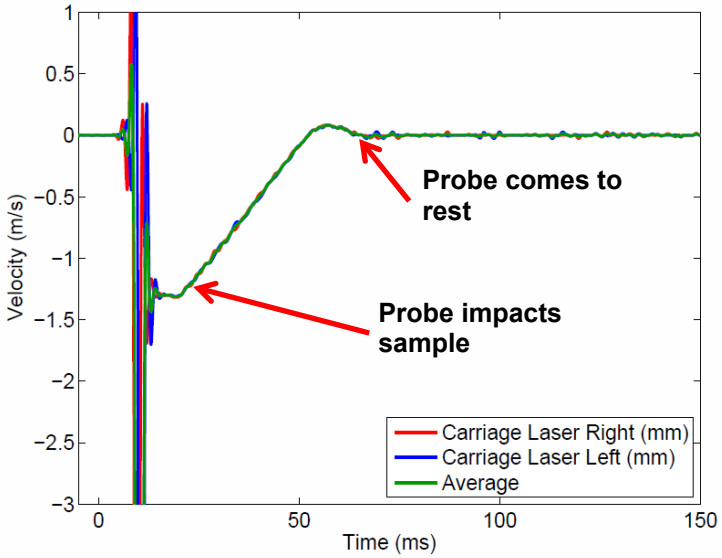

Figure 26: Velocity *vs.* Time Data from Test 9; Probe Did Not Fully Penetrate Sample 6

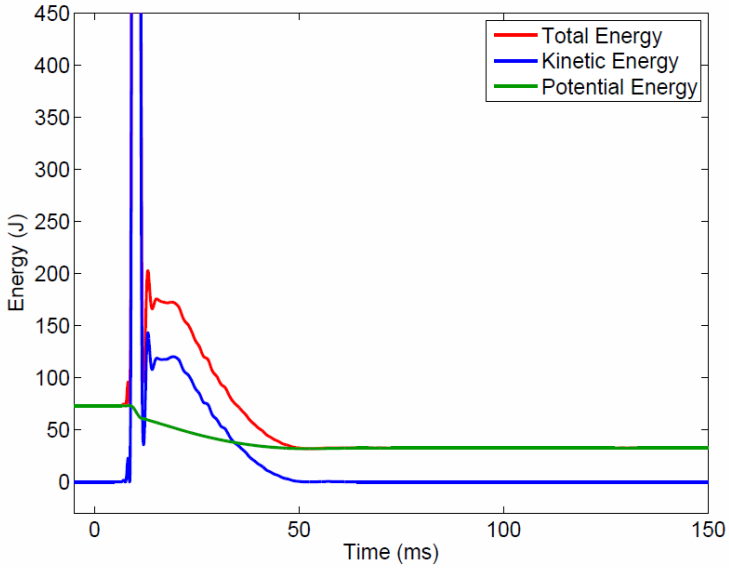

Figure 27: Energy *vs.* Time Data from Test 9; Probe Did Not Fully Penetrate Sample 6

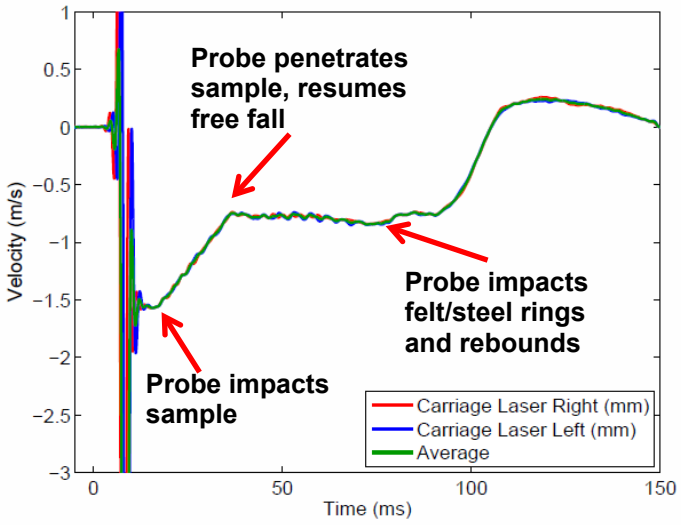

Figure 28: Velocity *vs.* Time Data from Test 6; Probe Fully Penetrated Sample 3

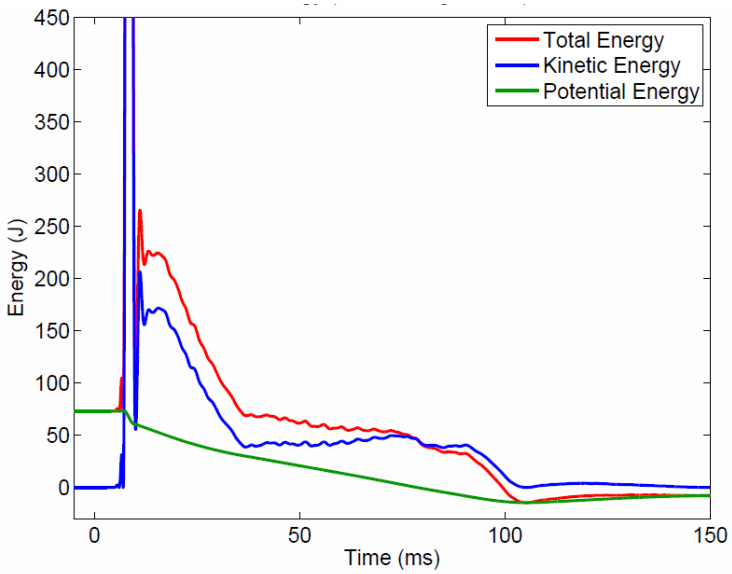

Figure 29: Energy *vs.* Time Data from Test 6; Probe Fully Penetrated Sample 3

The results followed fairly consistent patterns. In cases where the probe did not penetrate the sample, the velocity and kinetic energy of the carriage increased up until the point of impact with the sample. After impact, the velocity and kinetic energy of the carriage decreased quickly to zero. However, because the probe never reached the felt and steel stop rings, the potential energy remained positive. In cases where the probe did penetrate the sample, the kinetic energy and velocity of the sample again decreased quickly after the probe impacted the sample, but after the sample split into two pieces, the velocity and kinetic energy of the carriage increased again until impact with the felt and steel stops. In all cases where the probe fully penetrated the sample, it was noted that the sample split into two pieces after the probe partially penetrated the sample.

The average reading from the two accelerometers on the carriage indicated when the probe contacted the sample and when either the probe stopped or the sample broke. Figures 30 and 31

show the total energy of the carriage in the impact tests, grouped according to whether or not the samples fractured.

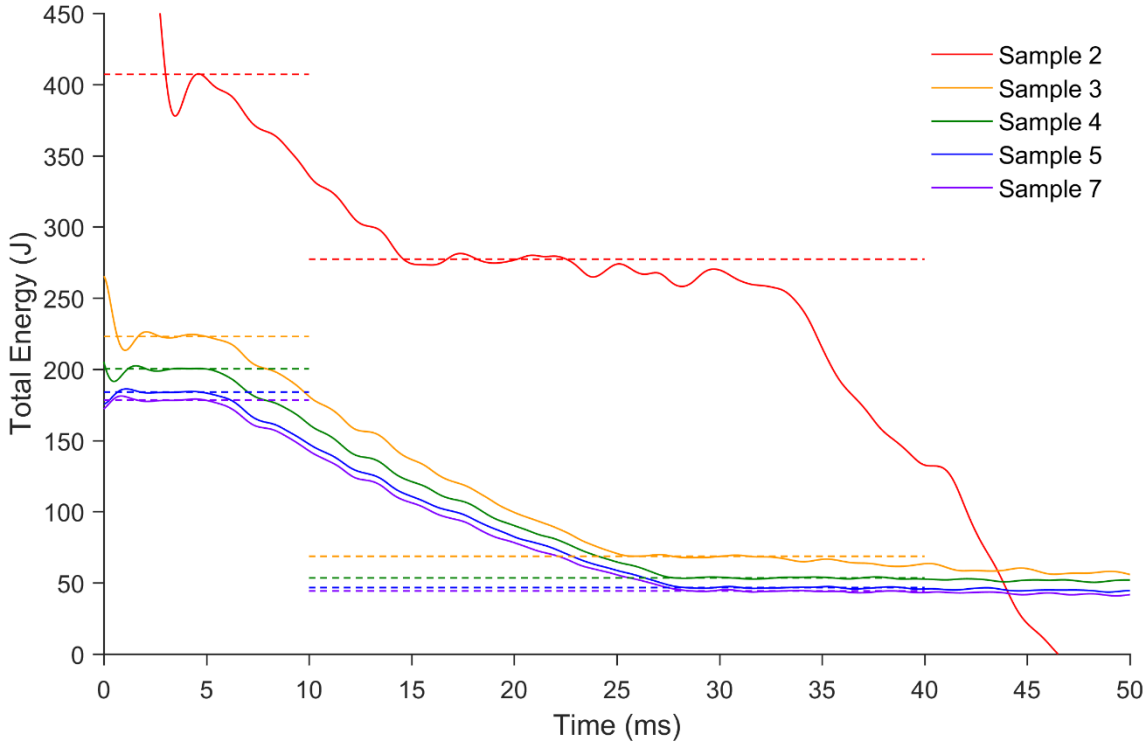

Figure 30: Total Energy from Tests of Samples that Broke

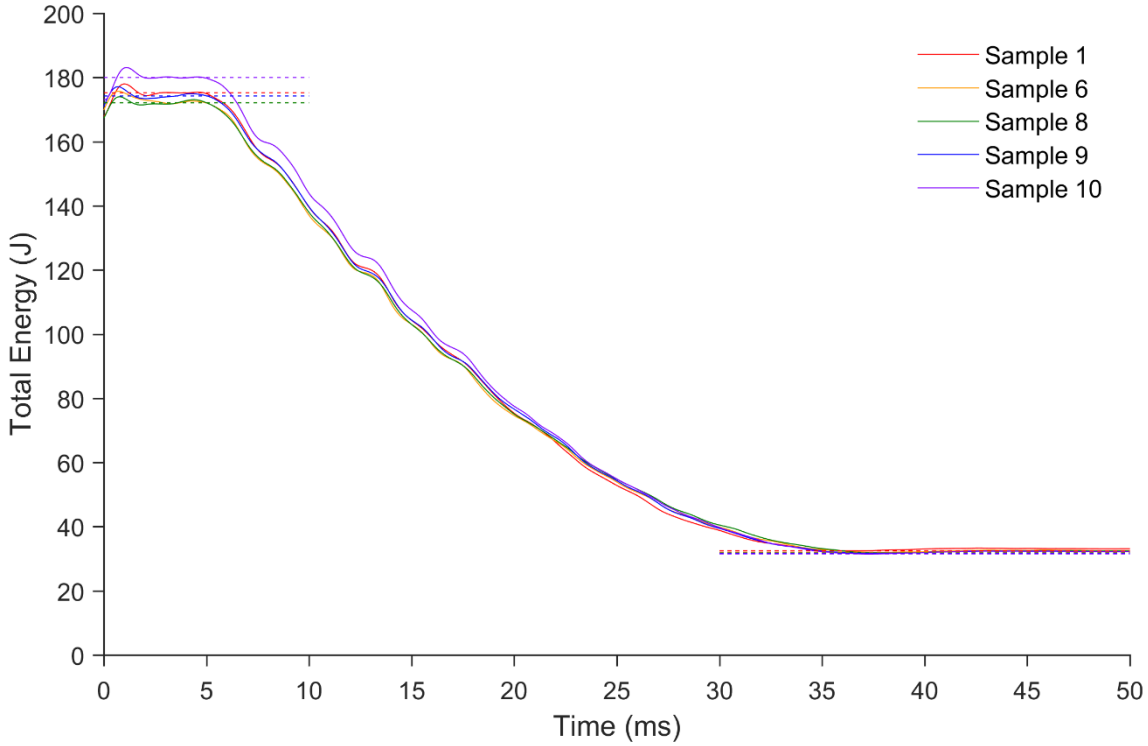

Figure 31: Total Energy from Tests of Samples that Remained Intact

The displacement sensors registered when the carriage came into visible range; there was significant noise at this point that translated through to the calculated energy (Fig. 27 and 29). In all but one test (test 5, sample 2), the energy stabilized before impact, indicating a measurable period of free-fall. The velocity of the probe before it impacted sample 2 was greater than for the other samples, and the displacement sensors did not have time to stabilize before impact; however, the energy absorption was consistent with the other samples that broke, so sample 2 is included in the summary statistics and plots. The energy decreased after impact as the probe moved through the sample and encountered resistance; it leveled out when the sample broke and the probe resumed free-fall (Fig. 30) or when the probe stopped (Fig. 31). The average total energy of the carriage during the approximately level periods is indicated in Figures 30 and 31 with dashed lines. The difference in the total energy before impact and after the sample broke or the probe stopped is the energy absorbed by the sample.

The depth to which the probe penetrated before it broke the sample or stopped was measured with a micrometer depth gage. The energy absorbed by each sample is plotted against the penetration depth in Figures 32 and 33. A linear fit to the data serves as an average that accounts for variation in the drop height and its effect on the energy and penetration depth. The fit lines are not statistically significant; therefore, no trends may be inferred from them. The lines only serve to define representative average energy values for the mean penetration depths in each data set.

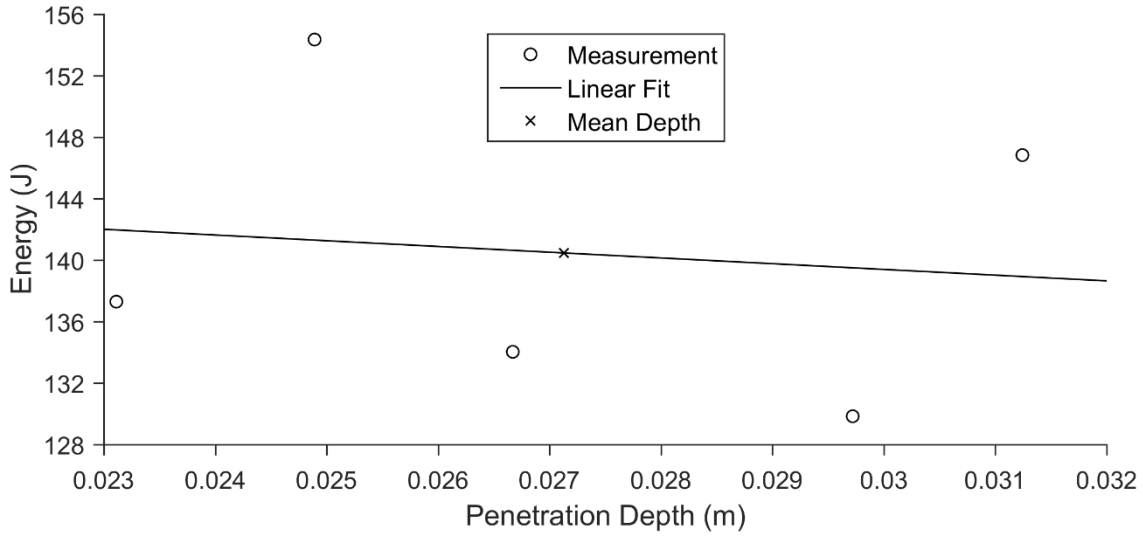

Figure 32: Energy Absorbed by Samples that Broke

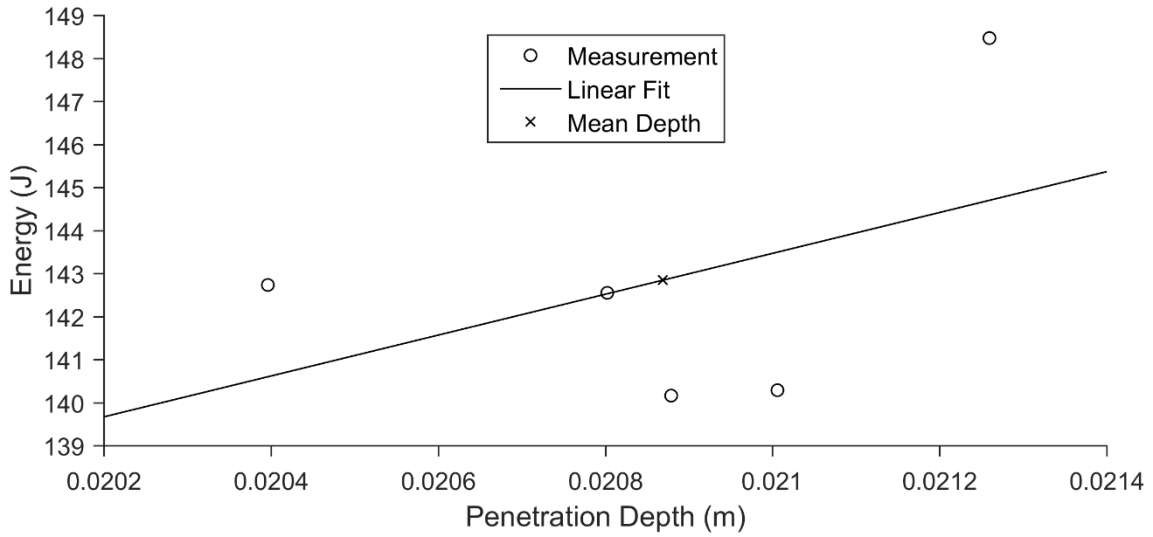

Figure 33: Energy Absorbed by Samples that Remained Intact

The mean penetration depth for either final condition of the sample is given in Table 10 with the energy value from the fit line at this depth. These points are plotted in Figures 32 and 33.

Table 10: Energy Absorption and Penetration Depth of Impact Tests

	Condition	SI Unit	Customary Unit
Mean Penetration Depth	Broken	27.1 mm	1.068 in
	Intact	20.9 mm	0.822 in
Energy at Mean Depth	Broken	140 J	104 ft-lb
	Intact	143 J	105 ft-lb

Figure 34 shows the full range of probe penetration depths as they relate to the initial height of the carriage and the resulting state of the sample. There is uncertainty in the energy required to break a sample. The samples that broke had a wide range of drop heights and significant variation in the penetration depth at which the sample cracked. The depths measured from samples that broke are significantly greater than for samples that remained intact, even with similar drop heights. This implies that there is bias in the measurement technique resulting from the difficulty of ascertaining the probe location from the marks in the samples. The samples that remained intact were tested close to the drop height at which they would have broken, so there is little scatter in the associated data. The points for these samples are clustered in the lower-left corner of Figure 34.

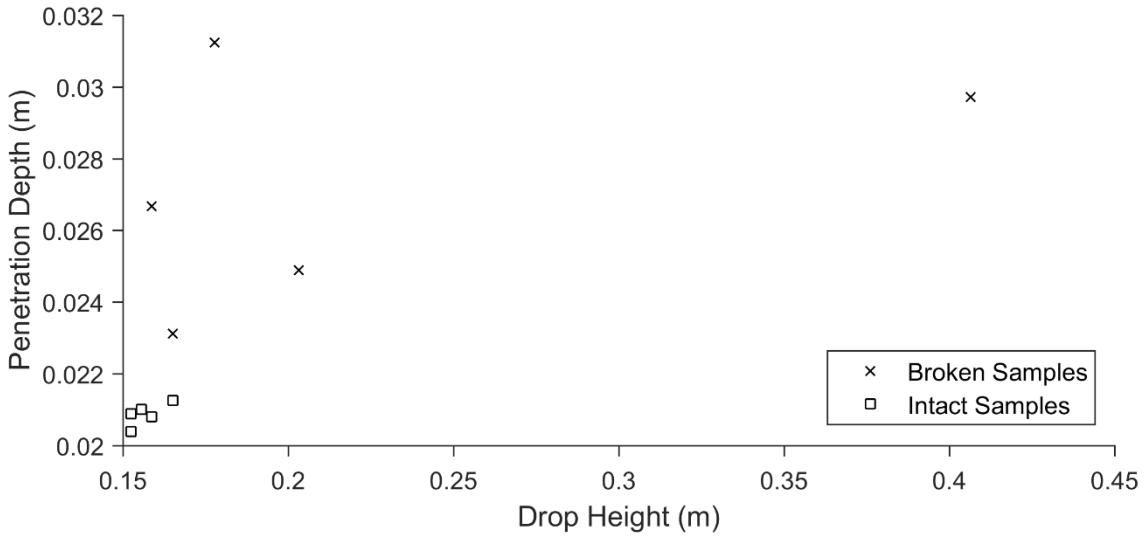

Figure 34: Relationship Between Penetration Depth and Drop Height

The energy absorbed by each sample is plotted against the drop height in Figure 35. The energy values are more consistent than the penetration depths in Figure 34 because the probe position and velocity measurements are less sensitive to the fracture of the sample. The energy values for the intact samples fall within the range of values for the fractured samples. The majority of the tests involved drop heights between 0.15 and 0.20 meters. Test 5 (on sample 2) began at a much greater height (0.41 meters) and does not fit the trend of the other tests. The discrepancy is attributed to uncertainty in the energy measurement, as was noted previously.

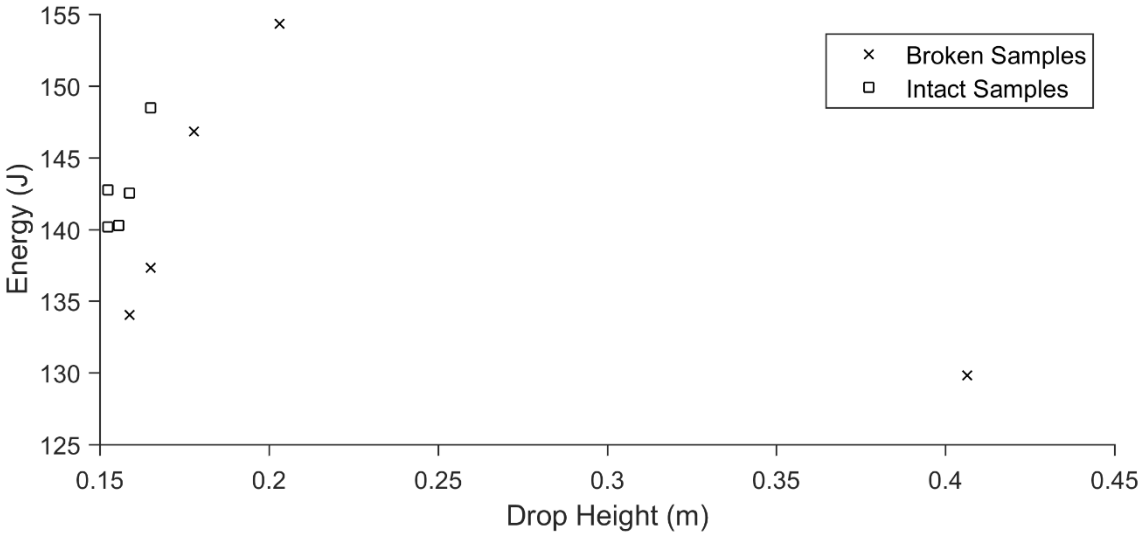

Figure 35: Relationship Between Energy Absorbed and Drop Height

4.4. Validation of Failure Criteria

A simulation of a probe impacting a block of material 9927092 is performed to validate the failure criteria for use in impact conditions. The dimensions of the probe, block, and support plate all match the actual test conditions. The model is simplified with one symmetry plane; this keeps the size of the model manageable while allowing it to capture more detailed failure modes than a quarter-symmetric model. The foam block and steel probe are modeled entirely with

hexahedral elements. The support plate is modeled with quadrilateral elements and has all of the nodes constrained, making it a rigid surface for contact. The probe has an elastic portion that contacts the block; behind this is a rigid portion to which two beam elements are attached. The uppermost beam element pushes the probe and measures the required force. The following figures illustrate the mesh. The characteristics of the mesh are given in Table 11.

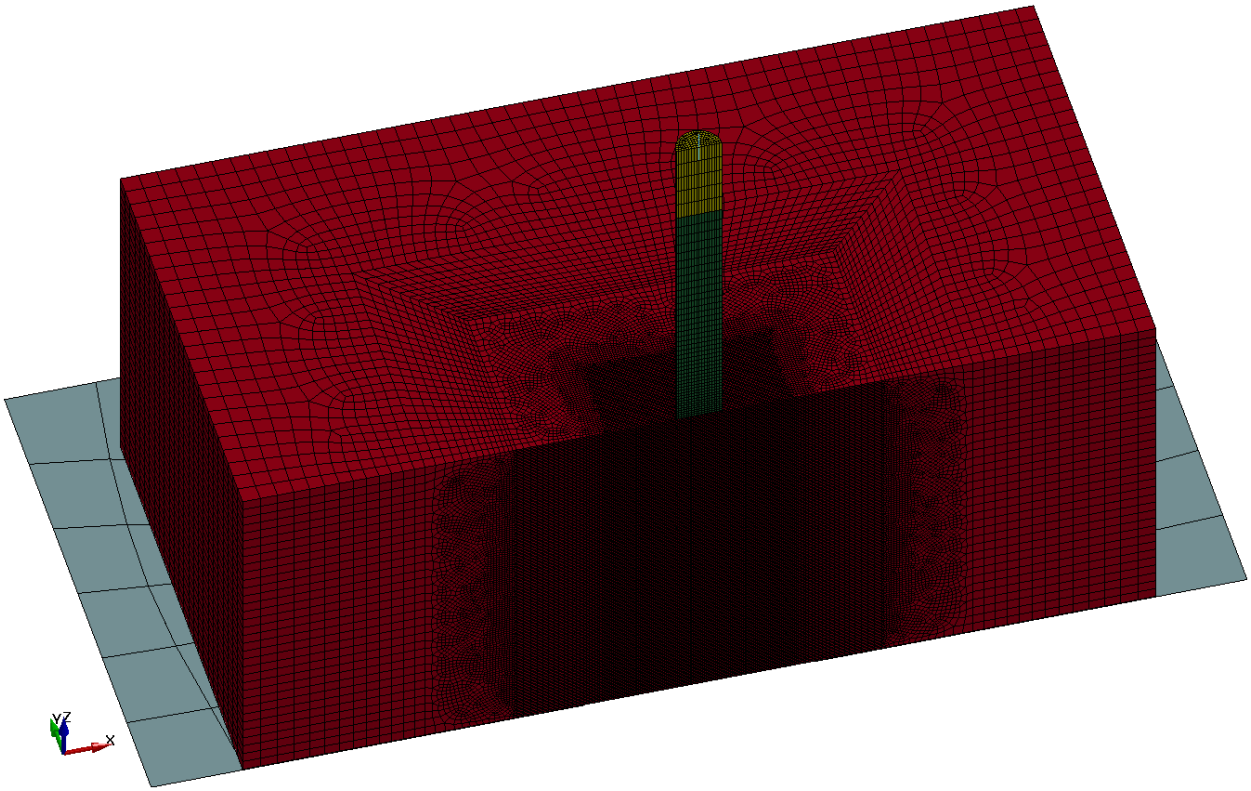

Figure 36: Finite Element Model of Foam Block to Simulate Impact Test

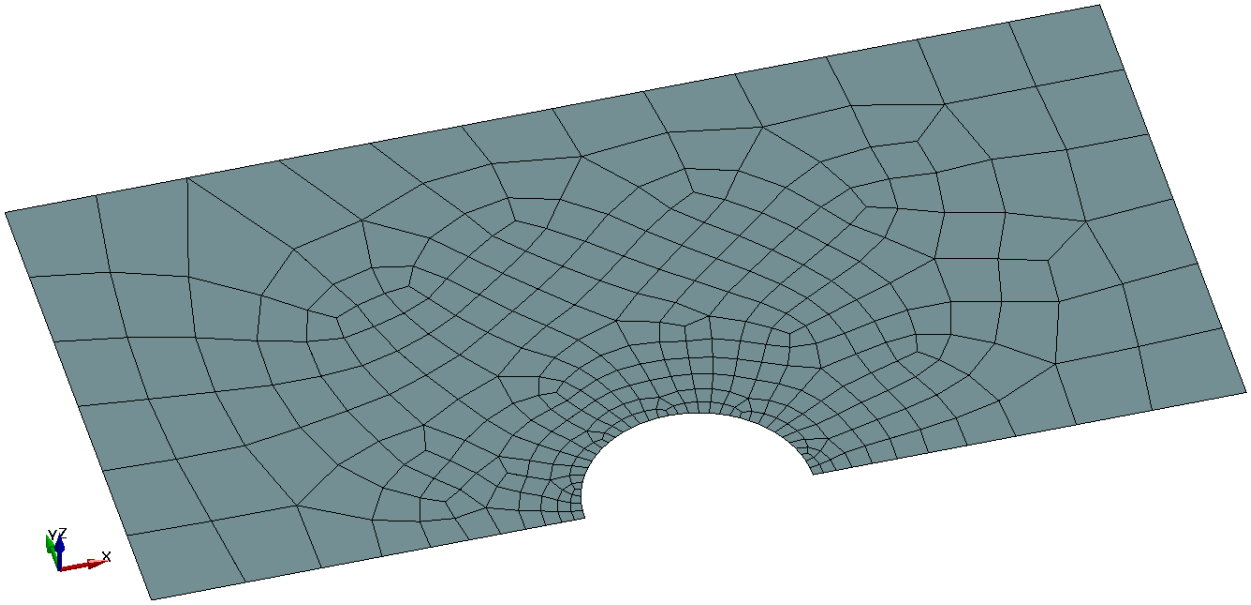

Figure 37: Quadrilateral Mesh of Rigid Support Plate

Table 11: Characteristics of Foam Block Model for Impact Simulations

	Constant Velocity Probe	Inertial Probe
Number of Elements	2,132,397	2,131,740
Minimum Side Length	254E-6 m 0.0100 in	254E-6 m 0.0100 in
Maximum Aspect Ratio	10.63	8.36
Minimum Taper Ratio	0.60	0.60
Maximum Skew Angle	49.3°	49.3°
Maximum Warp Angle	3.5°	3.5°
Maximum Twist Angle	19.7°	19.7°
Minimum Jacobian Ratio	0.21	0.21

The probe and the support plate are modeled as AISI type O1 tool steel with the linear elastic properties in Table 12.

Table 12: Properties of AISI Type O1 Tool Steel

Property	Symbol	Ref.	SI Unit		Customary Unit	
Density	ρ	12	7830	kg/m^3	733E-6	$lb \cdot s^2/in^4$
Modulus of Elasticity	E	12	214E9	Pa	31.0E6	psi
Poisson's Ratio	ν	12	0.3		0.3	

If the only failure criterion that triggers element erosion is the maximum shear strain of 0.0543 that correlates the model to the uniaxial compression data, the simulation of probe penetration only requires 4 Joules to reach the mean displacement from the tests. This is only 3% of the energy measured in the tests for the same displacement. Consequently, the 9927092 material is given a combination of failure criteria in LS-DYNA such that element erosion only occurs if (1) the maximum shear strain is exceeded and a state of positive mean stress exists (positive triaxiality), or (2) the minimum principal true strain is less than -2.3 (compressive engineering strain greater than 0.9) such that erosion occurs prior to element inversion. The combined failure criteria produce the results that are presented in this section.

The probe is first driven at a constant velocity of 10 meters per second. The force is integrated to calculate the work done by the probe (Fig. 38). The probe completely penetrates the block while doing 162 Joules of work. It is observed from the test results (Table 9) that the probe did not completely penetrate any of the samples without breaking them, and that the tests in which the probe stopped in the sample had similar drop heights and penetration depths (Fig. 34). For these reasons, the simulation is compared to the test results for samples that remained intact (Table 10). At the mean depth observed in the impact tests (Fig. 39), the energy imparted by the probe is 89 Joules. This is 38% less than the energy (143 Joules) calculated from the test results; therefore, the material model is conservative when applied to impact conditions. Additional results are presented below to confirm this conclusion.

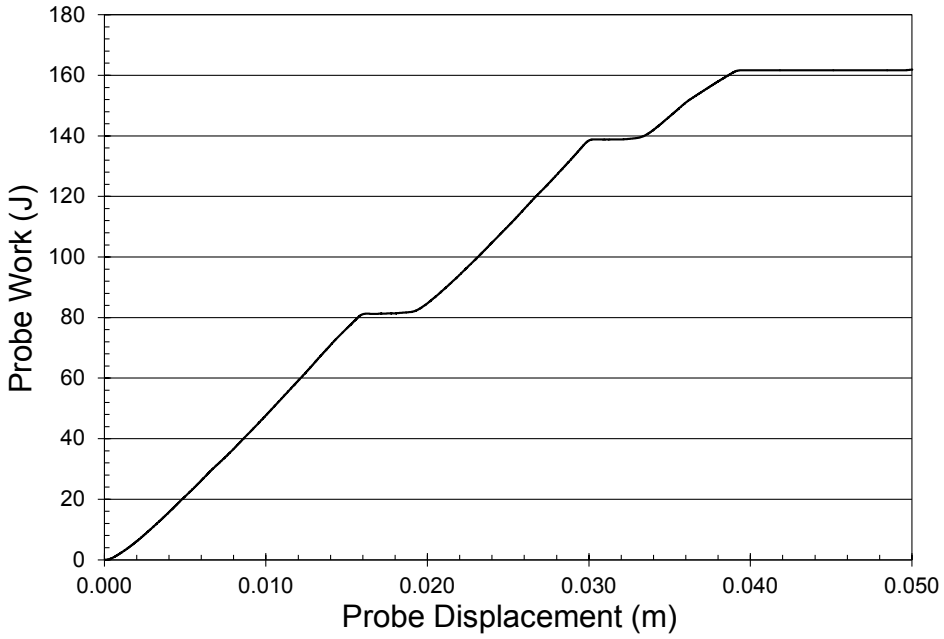

Figure 38: Probe Work as a Function of Displacement Through the Block

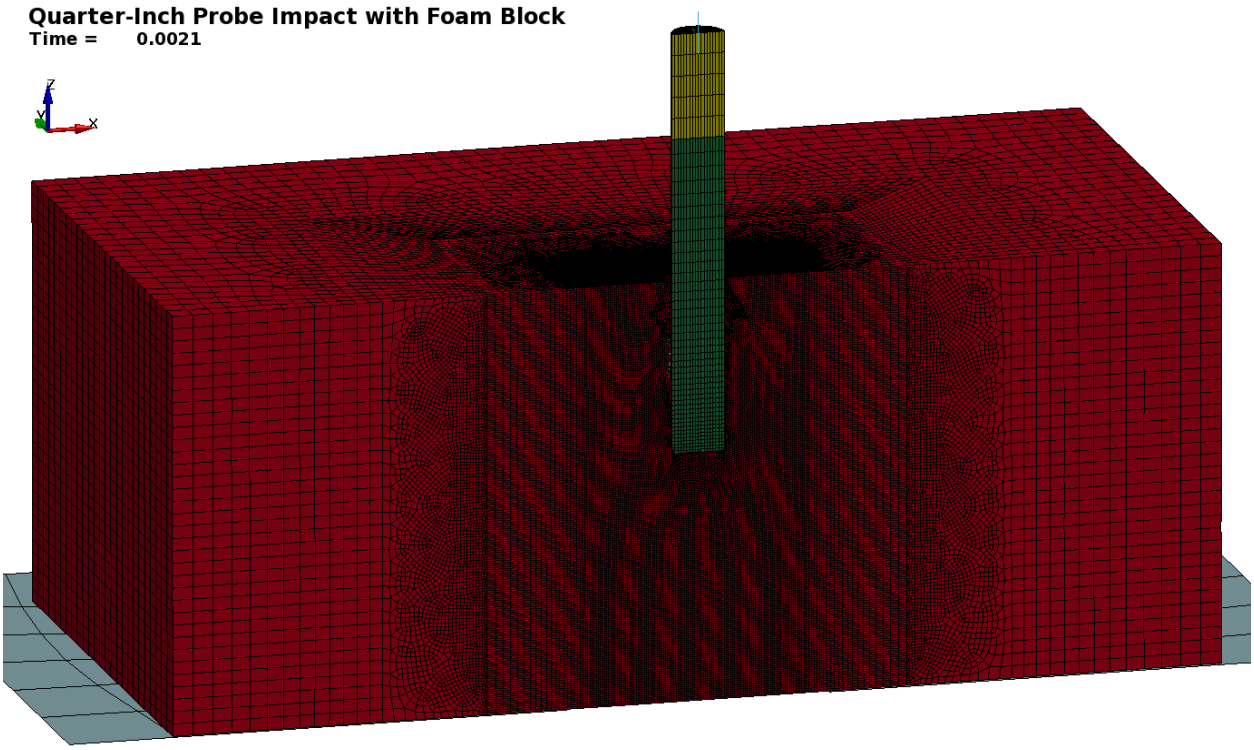

Figure 39: Probe Penetration of 0.0209 m at Constant Velocity

To demonstrate that the probe penetration simulation is conservative with diminishing velocity, the elastic portion of the probe is given the same mass as the carriage on the drop table and allowed to impact the block driven by its own inertia and gravity. The same gravitational constant (6.5 meters per second squared) that was used to calculate the potential energy from the displacement data is applied to the probe. The potential energy of the probe in this acceleration field is 19 joules relative to the mean penetration depth from the tests. The difference between the potential energy and the total energy of 143 joules that corresponds to the mean depth in the

test data is 124 joules. This is the initial kinetic energy of the probe. Equation 8 relates the kinetic energy to mass and velocity. Given the kinetic energy and the mass of the probe, the initial velocity is determined by Equation 9 to be 1.33 meters per second. The model of the probe driven by inertia and gravity is shown in Figure 40.

$$K = \frac{1}{2}mv^2 \tag{8}$$

$$v = \sqrt{\frac{2K}{m}} \tag{9}$$

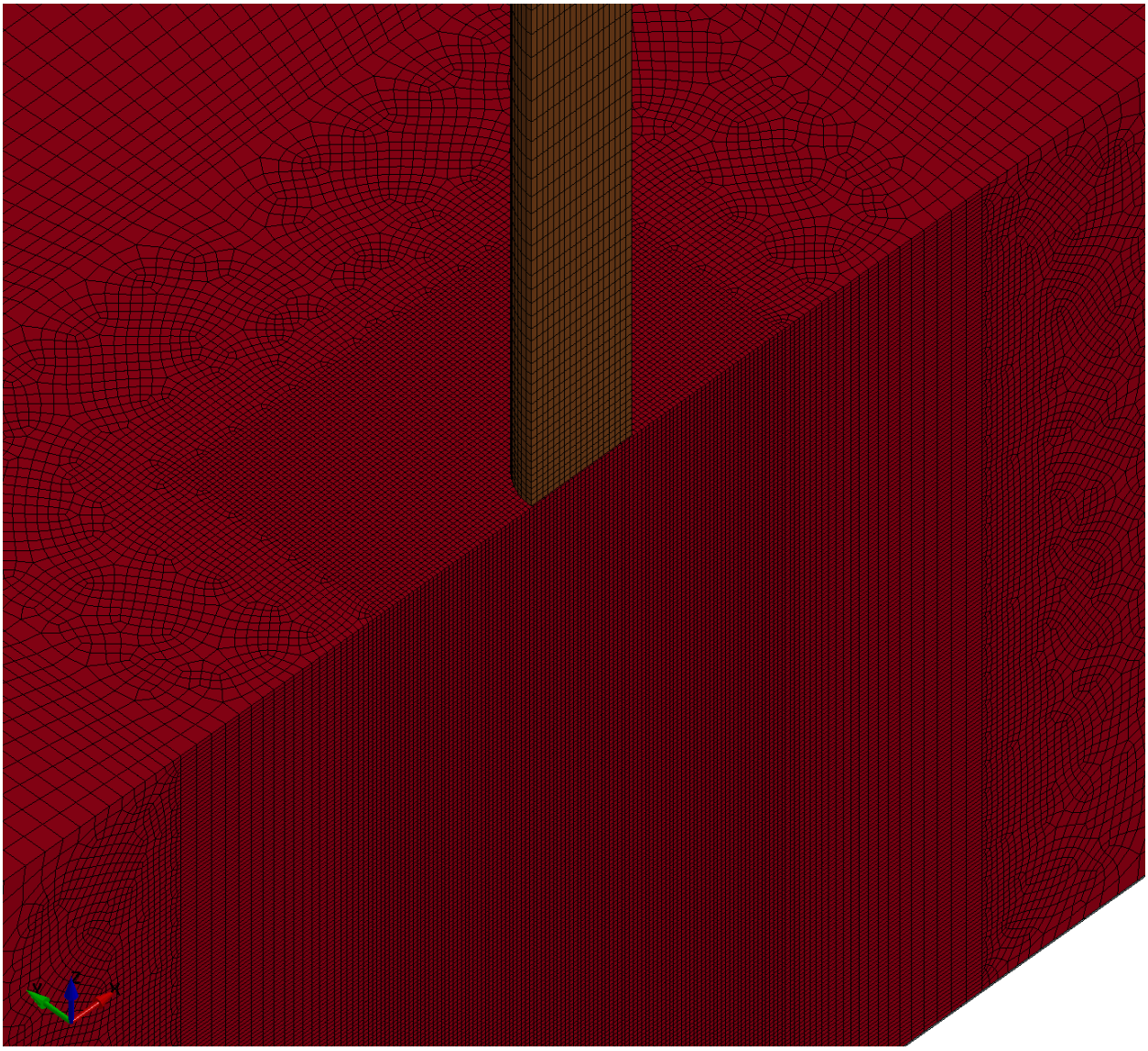

Figure 40: Model for Impact Simulations with Probe Driven by Initial Energy

With the correct initial kinetic energy applied to the probe and the acceleration field in place to produce the potential energy, the simulation mimics the test conditions. The results of this simulation are presented in Table 13. Figures 41 and 42 show the maximum displacement attained by the probe. It is 31% greater than the mean penetration depth from tests in which samples remained intact, so the model over-estimates the damage for a given initial energy.

Equivalently, it under-predicts the energy absorbed by the foam at a given penetration depth. Therefore, the model is conservative for conditions that closely resemble the tests, including velocity that diminishes to zero.

Table 13: Results of Simulation with Probe Driven by Initial Energy

Result	SI Unit		Customary Unit		Fraction of Test Result	Fraction of Energy Absorbed
Time	40.9	ms	0.040920	s		
Displacement	27.3	mm	1.073	in	131%	
Initial Kinetic Energy	124	J	91	ft-lb		83%
Potential Energy	25	J	18	ft-lb		17%
Energy Absorbed	149	J	110	ft-lb	104%	

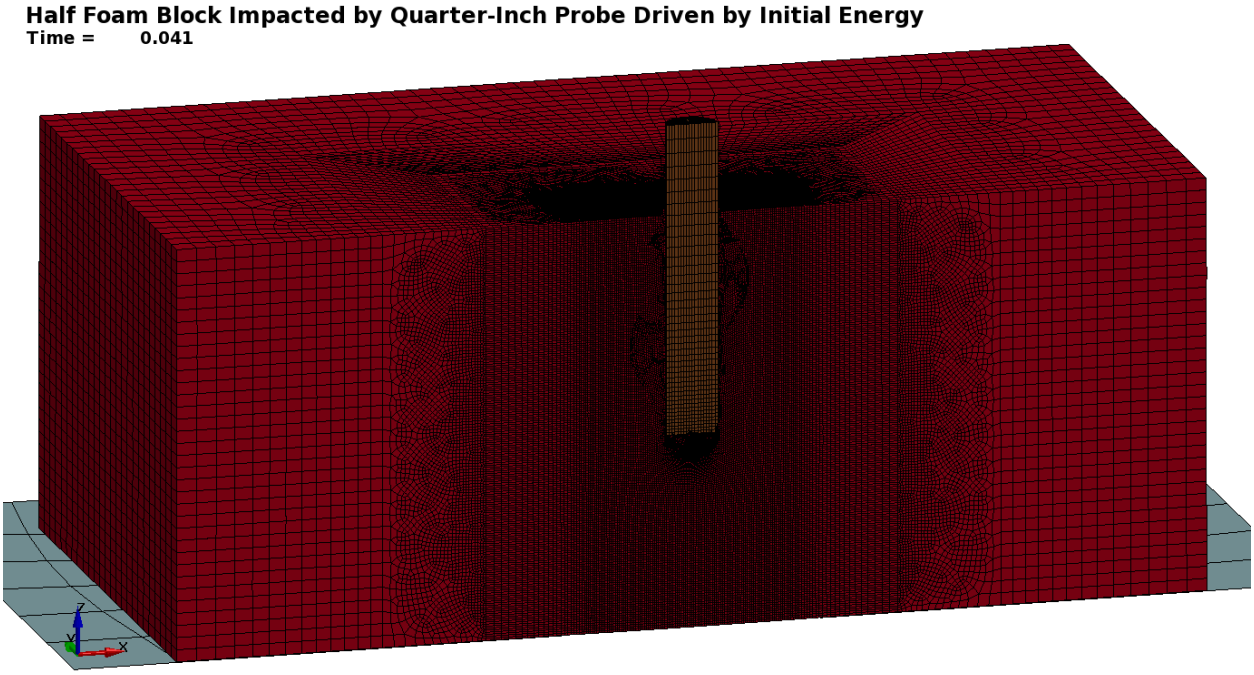

Figure 41: Maximum Probe Displacement in Simulation with Probe Driven by Initial Energy

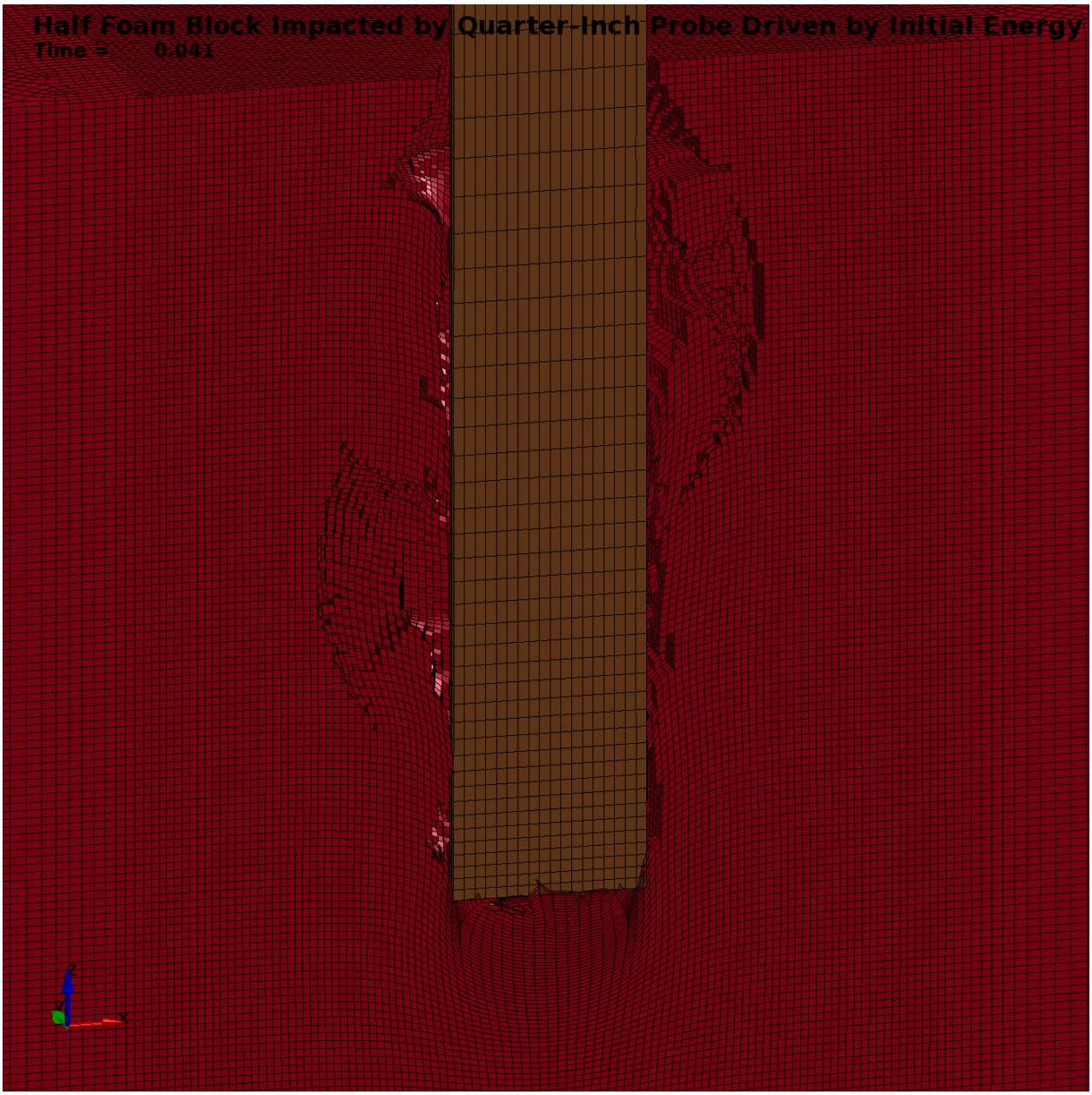

Figure 42: Close-up View of Probe at Maximum Displacement of 27.3 Millimeters

Figure 43 plots the total energy of the probe with the kinetic and potential components of energy. The energy absorbed by the foam is equal to the decrease in the total energy of the probe. The value of 149 Joules in Table 13 is 4% greater than the predicted energy that is used to determine the initial kinetic energy for this simulation; this is because the probe penetrates farther and consumes additional potential energy.

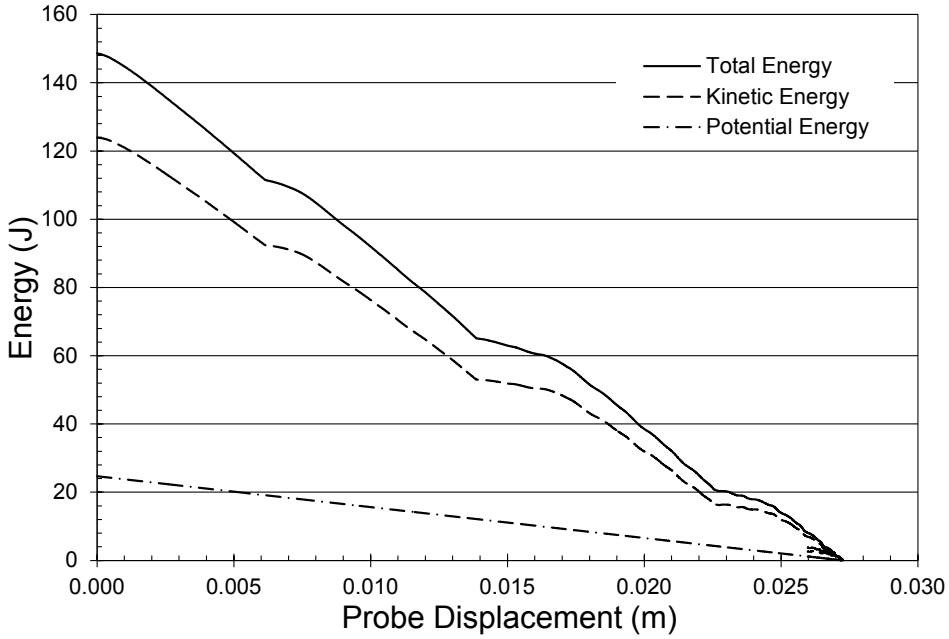

Figure 43: Energy Absorbed by Foam in Simulation with Probe Driven by Initial Energy

5. RECOMMENDATIONS

The material model for 9927092 syntactic foam may be applied to other simulations. It is simple enough to be implemented in a variety of simulation tools. With additional study it may be possible to refine the failure model for material 9927092 and correlate the results of the impact simulation more closely with the impact test data.

The results of any simulation are approximate. If a high degree of accuracy is required, tests of encapsulated components may be needed to quantify the energy absorbed during impact. Refining the models near the locations of the impacts would improve the accuracy of the simulations. When a probe penetrates the encapsulating foam, the elements in front of the probe compress severely and those around the perimeter fail in shear. Each element averages out the response of the material within its volume. The elements around the perimeter of the probe average the high shear strain at the edge the probe with the diminished strain farther away. Therefore, accuracy in puncture analyses is strongly dependent on mesh size. If the mesh is refined, it is advisable to measure the rate of convergence of the model with respect to the number of elements.

6. CONCLUSIONS

The material properties of 9927092 syntactic foam are summarized in Table 14. The moduli of elasticity have been calculated from experimental data. The relationship between true yield stress and true plastic strain is plotted in Figure 5 for tension and Figure 22 for compression. The curves of true yield stress *vs.* true plastic strain have been scaled to correlate simulation results to test results. The numerical values for the correlated curves are tabulated in Appendix A. The maximum shear strain is selected such that simulations of uniaxial tests fail close to the strains observed in tests.

Table 14: Properties of 9927092 Epoxy-Encapsulated Glass Microballoons

Property	Symbol	Ref.	SI Unit		Customary Unit	
Density	ρ	7	770	kg/m^3	72.1E-6	$lb \cdot s^2/in^4$
Modulus of Elasticity in Tension	E		3.79E9	Pa	550E3	psi
Modulus of Elasticity in Compression	E_c		2.04E9	Pa	296E3	psi
Poisson's Ratio	ν	8	0.36		0.36	
Maximum Shear Strain	$\varepsilon_{s,max}$		0.0543		0.0543	

Uncertainty is introduced into the simulation results through geometric simplifications, finite element discritization, material property development including sample preparation and testing, assumptions about the properties of non-structural materials, simplified constitutive models and failure criteria, simplified probe geometry (as compared to actual tools), and assumed constraint conditions; many other sources of uncertainty exist. Conservative assumptions are employed to bound some of these uncertainties. For example, the probe puncture simulation utilizing the 9927092 material model predicts less energy absorption than what is substantiated through testing.

A combination of failure criteria is recommended for element erosion in probe penetration simulations. Elements are removed from the simulation if two of the following three criteria are met: (1) the maximum shear strain exceeds 0.0543; (2) the mean stress (or triaxiality) is positive; and (3) the minimum principal true strain is less than -2.3. This causes the elements of material 9927092 to absorb less energy in simulations than in tests; therefore, the failure criteria are conservative.

REFERENCES

1. Sandia National Laboratories, 9927092, "Encapsulation, Glass Microsphere-Filled, Rubber Toughened Epoxy," Issue M, April 1997.
2. Sandia National Laboratories, 2140646, "CTBN-DGEBA Epoxy Reaction Product (10-Percent)," Issue H, September 2004.
3. Sandia National Laboratories, 6090014, "Filler, Hollow Glass Microspheres," Issue G, August 2007.
4. Sandia National Laboratories, 4604020, "Diethanolamine Curing Agent," Issue AB, August 2010.
5. Sandia National Laboratories, 2140285, "Epoxy Resin," Issue AN, August 2011.
6. Sandia National Laboratories, 4160030, "Carboxyl-Terminated Nitrile Elastomer," Issue M, May 2011.
7. Sandia National Laboratories, "828/CTBN/DEA/GMB," http://www.sandia.gov/polymer-properties/828_CTBN_DEA_GMB.html, Accessed 14 April 2015.
8. Guess, T. R., Wischmann, K. B., and Stavig, M. E., SAND92-2768, "Tensile Properties of Epoxy Encapsulants," Sandia National Laboratories, 1992.
9. LSTC, "From Engineering to True Strain, True Stress," 2002, http://www.dynasupport.com/howtos/material/from-engineering-to-true-strain-true-stress/, Accessed 28 September 2015.
10. Shigley, J. E., and Mischke, C. R., *Mechanical Engineering Design*, McGraw-Hill, 2001.
11. Department of Defense, MIL-HDBK-5J, "Metallic Materials and Elements for Aerospace Vehicle Structures," 31 January 2003.
12. MatWeb, "AISI Type O1 Oil-hardening Tool Steel, Oil Quenched at 800°C, Tempered at 425°C," http://www.matweb.com/search/DataSheet.aspx?MatGUID=42da7db7f74041a98f3ee0239b4c6ac6&ckck=1, Accessed 28 September 2015.

APPENDIX A: YIELD STRESS VERSUS PLASTIC STRAIN FOR MATERIAL 9927092

The correlated curves of true yield stress *vs.* true plastic strain for material 9927092 are presented in Tables 15 and 16.

Table 15: Yield Stress Curve for Material 9927092 in Tension

Effective Plastic Strain	True Yield Stress (Pa)	Effective Plastic Strain	True Yield Stress (Pa)	Effective Plastic Strain	True Yield Stress (Pa)
0.000E0	1.764E7	7.628E-5	2.588E7	3.196E-4	3.373E7
9.260E-8	1.764E7	8.108E-5	2.612E7	3.289E-4	3.396E7
2.925E-7	1.790E7	8.604E-5	2.636E7	3.383E-4	3.418E7
6.025E-7	1.816E7	9.114E-5	2.660E7	3.478E-4	3.440E7
1.026E-6	1.841E7	9.641E-5	2.684E7	3.573E-4	3.462E7
1.564E-6	1.867E7	1.018E-4	2.708E7	3.670E-4	3.484E7
2.221E-6	1.893E7	1.074E-4	2.732E7	3.767E-4	3.506E7
2.999E-6	1.918E7	1.131E-4	2.755E7	3.865E-4	3.528E7
3.899E-6	1.944E7	1.190E-4	2.779E7	3.964E-4	3.550E7
4.926E-6	1.969E7	1.250E-4	2.802E7	4.063E-4	3.572E7
6.080E-6	1.995E7	1.311E-4	2.826E7	4.163E-4	3.594E7
7.364E-6	2.020E7	1.375E-4	2.849E7	4.263E-4	3.616E7
8.780E-6	2.045E7	1.439E-4	2.873E7	4.364E-4	3.638E7
1.033E-5	2.071E7	1.505E-4	2.896E7	4.466E-4	3.660E7
1.201E-5	2.096E7	1.573E-4	2.919E7	4.568E-4	3.682E7
1.384E-5	2.121E7	1.642E-4	2.942E7	4.670E-4	3.704E7
1.580E-5	2.146E7	1.712E-4	2.965E7	4.773E-4	3.726E7
1.790E-5	2.171E7	1.784E-4	2.989E7	4.876E-4	3.748E7
2.015E-5	2.196E7	1.857E-4	3.012E7	4.979E-4	3.769E7
2.254E-5	2.221E7	1.931E-4	3.035E7	5.083E-4	3.791E7
2.507E-5	2.246E7	2.007E-4	3.058E7	5.186E-4	3.813E7
2.775E-5	2.271E7	2.084E-4	3.080E7	5.290E-4	3.835E7
3.058E-5	2.296E7	2.162E-4	3.103E7	5.394E-4	3.857E7
3.355E-5	2.320E7	2.242E-4	3.126E7	5.497E-4	3.878E7
3.668E-5	2.345E7	2.323E-4	3.149E7	5.601E-4	3.900E7
3.995E-5	2.370E7	2.405E-4	3.171E7	5.705E-4	3.922E7
4.338E-5	2.394E7	2.489E-4	3.194E7	5.808E-4	3.944E7
4.696E-5	2.419E7	2.573E-4	3.217E7	5.911E-4	3.966E7
5.069E-5	2.443E7	2.659E-4	3.239E7	6.014E-4	3.987E7
5.457E-5	2.468E7	2.746E-4	3.262E7	6.116E-4	4.009E7
5.860E-5	2.492E7	2.834E-4	3.284E7	6.218E-4	4.031E7
6.279E-5	2.516E7	2.923E-4	3.306E7	6.320E-4	4.053E7
6.713E-5	2.540E7	3.013E-4	3.329E7	6.422E-4	4.053E7
7.163E-5	2.564E7	3.104E-4	3.351E7		

Table 16: Yield Stress Curve for Material 9927092 in Compression

Effective Plastic Strain	True Yield Stress (Pa)	Effective Plastic Strain	True Yield Stress (Pa)	Effective Plastic Strain	True Yield Stress (Pa)
0.000E0	3.568E7	5.984E-4	5.288E7	3.012E-3	6.624E7
3.489E-7	3.622E7	6.394E-4	5.334E7	3.118E-3	6.655E7
1.412E-6	3.677E7	6.821E-4	5.379E7	3.228E-3	6.687E7
3.228E-6	3.731E7	7.263E-4	5.424E7	3.339E-3	6.717E7
5.834E-6	3.784E7	7.723E-4	5.469E7	3.454E-3	6.748E7
9.267E-6	3.838E7	8.199E-4	5.513E7	3.571E-3	6.777E7
1.356E-5	3.892E7	8.693E-4	5.557E7	3.692E-3	6.806E7
1.875E-5	3.945E7	9.203E-4	5.600E7	3.816E-3	6.834E7
2.487E-5	3.998E7	9.731E-4	5.643E7	3.944E-3	6.862E7
3.195E-5	4.051E7	1.028E-3	5.686E7	4.075E-3	6.888E7
4.002E-5	4.103E7	1.084E-3	5.728E7	4.211E-3	6.914E7
4.911E-5	4.156E7	1.142E-3	5.770E7	4.351E-3	6.939E7
5.925E-5	4.208E7	1.202E-3	5.812E7	4.497E-3	6.963E7
7.046E-5	4.260E7	1.264E-3	5.853E7	4.647E-3	6.985E7
8.278E-5	4.312E7	1.328E-3	5.894E7	4.804E-3	7.007E7
9.623E-5	4.363E7	1.393E-3	5.934E7	4.967E-3	7.027E7
1.108E-4	4.414E7	1.461E-3	5.974E7	5.138E-3	7.045E7
1.266E-4	4.465E7	1.530E-3	6.014E7	5.316E-3	7.062E7
1.436E-4	4.516E7	1.601E-3	6.053E7	5.504E-3	7.078E7
1.618E-4	4.566E7	1.674E-3	6.092E7	5.701E-3	7.091E7
1.813E-4	4.617E7	1.749E-3	6.130E7	5.908E-3	7.102E7
2.020E-4	4.667E7	1.826E-3	6.168E7	6.128E-3	7.110E7
2.241E-4	4.716E7	1.905E-3	6.206E7	6.361E-3	7.116E7
2.475E-4	4.766E7	1.986E-3	6.243E7	6.608E-3	7.119E7
2.722E-4	4.815E7	2.069E-3	6.280E7	6.871E-3	7.119E7
2.983E-4	4.863E7	2.154E-3	6.316E7	7.152E-3	7.115E7
3.257E-4	4.912E7	2.241E-3	6.352E7	7.453E-3	7.107E7
3.546E-4	4.960E7	2.330E-3	6.388E7	7.775E-3	7.095E7
3.850E-4	5.008E7	2.421E-3	6.423E7	8.120E-3	7.078E7
4.167E-4	5.055E7	2.514E-3	6.457E7	8.492E-3	7.055E7
4.500E-4	5.103E7	2.609E-3	6.492E7	8.893E-3	7.027E7
4.848E-4	5.150E7	2.706E-3	6.525E7	9.324E-3	6.992E7
5.211E-4	5.196E7	2.806E-3	6.559E7	9.756E-3	6.992E7
5.590E-4	5.242E7	2.908E-3	6.591E7		

DISTRIBUTION

1	MS0405	M. F. Pasik	00432
1	MS0557	D. M. Jones	01528
1	MS0899	Technical Library	09536 (electronic copy)
1	MS0958	M. J. Kelly	01833
1	MS1467	C. M. Waymire	03644


Sandia National Laboratories